STUDY OF STRESS PATHS IN ARCHING EFFECT USING FRICTIONAL STRAIN HARDENING AND SOFTENING IN FINE SAND

Alireza Abbasnejad*

Assistant Professor, University of Tabriz, Tabriz, Iran

abbasnejad@tabrizu.ac.ir

Mahyar Soltani

MSc Student, University of Tabriz, Tabriz, Iran

maahyarsoltani@gmail.com

Reception: 18/02/2023 **Acceptance**: 15/04/2023 **Publication**: 02/05/2023

Suggested citation:

Abbasnejad, A. and Soltani, M. (2023). **Study of Stress Paths in Arching Effect Using Frictional Strain Hardening and Softening in Fine Sand**. *3C TIC. Cuadernos de desarrollo aplicados a las TIC, 12(2)*, 15-58. https://doi.org/10.17993/3ctic.2023.122.15-58

https://doi.org/10.17993/3ctic.2023.122.15-58

ABSTRACT

Arching is one of the most common phenomena that occur in most geotechnical structures. To determine the properties and quality of this phenomenon, a physical model has been designed and constructed. The apparatus comprises rectangular trapdoors with different widths that can yield downward while stresses and deformations are recorded simultaneously. As the trapdoor starts to fail, the whole soil mass deforms elastically. However, after an immediately specified displacement, depending on the width of the trapdoor, the soil mass behaves plastically. This behavior of sand occurs due to the flow phenomenon and continues until the stress on the trapdoor is minimized. Then the failure process develops in the sand, and the measured stress on the trapdoor shows an ascending trend. This indicates a gradual separation of the yielding mass from the whole soil body. Finally, the flow process leads to the establishment of a stable vault of sand called the arching mechanism or progressive collapse of the soil body. To simulate this phenomenon with continuum mechanics, the experimental procedure is modeled in ABAQUS software using stress-dependent hardening in an elastic state and plastic strain-dependent frictional hardening-softening with Mohr Coulomb failure criterion applying user sub-routine. The results show that the experimental data have an acceptable corresponding to the numerical analysis data. So the selected soil behavior could indicate the main aspects of the arching effect, such as the flow that occurs in specific periods of strains. In the following, the stress path in p, q, and p, v space was extracted from numerical analysis, and the results have been discussed.

KEYWORDS

ABAQUS, Arching Effect, Stress Path, PIV, Frictional Strain Hardening and Softening, Fine Sand.

https://doi.org/10.17993/3ctic.2023.122.15-58

INDEX

https://doi.org/10.17993/3ctic.2023.122.15-58

1. INTRODUCTION

The arch phenomenon is one of the most important phenomena that we deal with in geotechnical engineering. The impact of this phenomenon can be clearly seen in underground and buried structures, so that the amount of force applied to the structure depends on the redistribution of the stress caused by overburden or overburden. Many scientists and researchers have worked in this field in a laboratory and theoretical manner and have written numerous articles. This phenomenon was first observed in the gunpowder storage silos belonging to the French army, and in 1895 John Sen presented the theory of silos. This phenomenon was shown for the first time in a scientific way by an experiment on sand with an open valve conducted by Terzaghi. It was proposed by him in geotechnical engineering. Usually, this phenomenon occurs in places where there are sudden differences in the type of materials in the soil mass. In other words, in the mass, two types of materials with a different modulus of elasticity come into contact and exchange stress with each other. In general, it can be said that arching occurs wherever there is a change of location in the soil mass enclosed between stable supports, whether horizontal or vertical. Also, this phenomenon can exist in all extents of deformation in the soil, so it starts with the occurrence of elastic shear deformations and continues until the irreversible (plastic) deformations and the breaking of parts of the soil mass.

To investigate the arching phenomenon in underground structures, Terzaghi conducted an experiment in which a horizontal valve was lowered. When it was moved, the amount of stress applied to the center of the valve was simultaneously read. Using the results of these experiments and assuming plastic behavior for soil, Terzaghi presented the theory of shear plates. In fact, by considering the balance of forces in the plastic state of the soil, Tarzaghi was able to make the arch phenomenon mathematically legal. After V. Finn, he modified the hypothesis related to Terzaghi's theory and considered the elastic state of the soil. In the following years, many experimental and numerical studies have been conducted to investigate the failure mechanisms of the soil mass above the tunnel (Atkinson and Potts, 1977; Jiang and Yin, 2012; Guo and Zhou, 2013; Han et al., 2017; Franza et al., 2018; Chen et al., 2018; Jin et al., 2021; Zheng et al., 2021). These studies play an important role in improving the understanding of the interaction between tunnels and soil and create a solid foundation for developing theoretical models. After that, the parameters of silo width and lateral stress ratio in Terzaghi theory were modified by many researchers based on model tests and numerical analyzes (Stein et al., 1989; Hendi, 1985; Chen et al., 2015; Zhang et al., 2016). Although many significant modifications have been made based on Terzaghi's loose earth pressure theory, most of the research has focused on shallow tunnels where the failure zone at the top of the tunnel extends to the ground surface when the soil mass is in a limited state. However, for deep tunnels, local failure occurs at the top of the tunnel according to many laboratory tests (Jacobs, 2016; Song et al., 2018) to evaluate the earth pressure on deep tunnels. Based on the existing theoretical models for the shallow tunnel, a limited height of the silo was further considered. Chen and Peng (2018) assumed that the height is 1.5 times the

https://doi.org/10.17993/3ctic.2023.122.15-58

radius of the tunnel based on the numerical results in the soft ground of Shanghai. The local failure height for the deep tunnel is related to the ground subsidence, the phenomenon of soil expansion (change), and the depth of the tunnel cover in the light of the previous study. Zhang et al. (2016) obtained a formula for calculating the local failure height caused by the construction of the deep jacked pipe, in which the relationship between the local failure height, the volume of loosened soils, and soil bulking factors are simultaneously considered, was taken. Zhang's method assumed that the shear bands start from the spring lines of the tunnel section. However, according to the numerical results of Lin et al. (2019), the shear bands developed diagonally from the bottom of the tunnel in the sandy ground. Therefore, the formula presented by Zhang et al. (2016), used to calculate the local failure height, is limited to sand.

However, the previous models for calculating the earth pressure in deep tunnels assumed that the soil mass above the failure zone was not disturbed by the construction of the tunnel and that the earth pressure applied above the failure zone is the stress caused by the weight of the soil above, in fact, soil arching in occurs above the failure zone, which leads to the transfer of earth pressure to both sides of the failure zone. When the arch-bearing capacity of the soil is greater than or equal to the weight of the soil above the failure zone, a cavity can be created above the failure zone. The failure zone is zero. Such an arching effect of the soil above the failure zone has been neglected by previous analytical approaches, which may consequently overestimate the earth pressure exerted on the silo. A new 3D model considering the arch effect above the fracture zone was developed by Chen et al. in 2019. To predict the confining pressure exerted on the surface of the deep shield tunnel. The calculated results by obtaining the new model agree with the experimental results. However, it is assumed that the earth pressure distribution in the loosened zone is uniform. The distribution of earth pressure on the tunnel can be different due to the difference in the distribution of earth losses caused by the construction of the tunnel. For the circular tunnel, Chen and Teng in 2018 pointed out that the vertical earth pressure distribution shows a concave curve; that is, it is smaller in the center line and increases with the increase of the horizontal distance from the center of the tunnel. However, the current tunnel design for tunnels generally assumes vertical earth pressure of uniform width. To reflect the uneven distribution of the vertical earth pressure in the tunnel, Chen and Teng in 2018 assumed that the vertical earth pressure on the tunnel conforms to the distribution of the Gaussian function, and then presented a formula for calculating the earth pressure. However, there is a relatively large error between the model results and the numerical analysis. Based on particle flow theory, Wu et al. in 2019 obtained a modified formula by assuming that the vertical earth pressure on the tunnel corresponds to a trapezoidal distribution. But, in fact, the vertical pressure distribution of the earth is a smooth concave curve.

In this article, in order to determine the characteristics and how this phenomenon occurs, a physical model has been designed and built that can model the arcing phenomenon in a laboratory. In this physical model, valves with different widths have

https://doi.org/10.17993/3ctic.2023.122.15-58

been installed to investigate the effect of valve width on the occurrence of this phenomenon. To determine the pattern of stress changes during the event of the arcing phenomenon, miniature stress gauges with a diameter of 14 mm have been used, and to determine the pattern of strain changes, the PIV method has been used. Also, numerical modeling of this phenomenon has been done in Abaqus software and the finite element method. To model the arch phenomenon, the hardening behavior dependent on the stress level in the elastic range and the hardening and softening depending on the plastic strain in the plastic range were used; for this purpose, a program was written in the form of a subroutine in the Fortran environment and then with the help of a compiler Visual Studio has been introduced to Abaqus software.

2. PHYSICAL MODEL

In this research, to model the arcing phenomenon, a physical model was designed and built to provide the ability to model the arcing phenomenon on a laboratory scale.

2.1. SOIL UNDER TEST

A type of non-sticky silty sand passed through a grade 10 sieve, with a constant humidity of 2% and a specific gravity of 2.62, was used for the experiments. The granulation diagram and characteristics of the soil used are presented in Fig. 1 and Table 1, respectively.

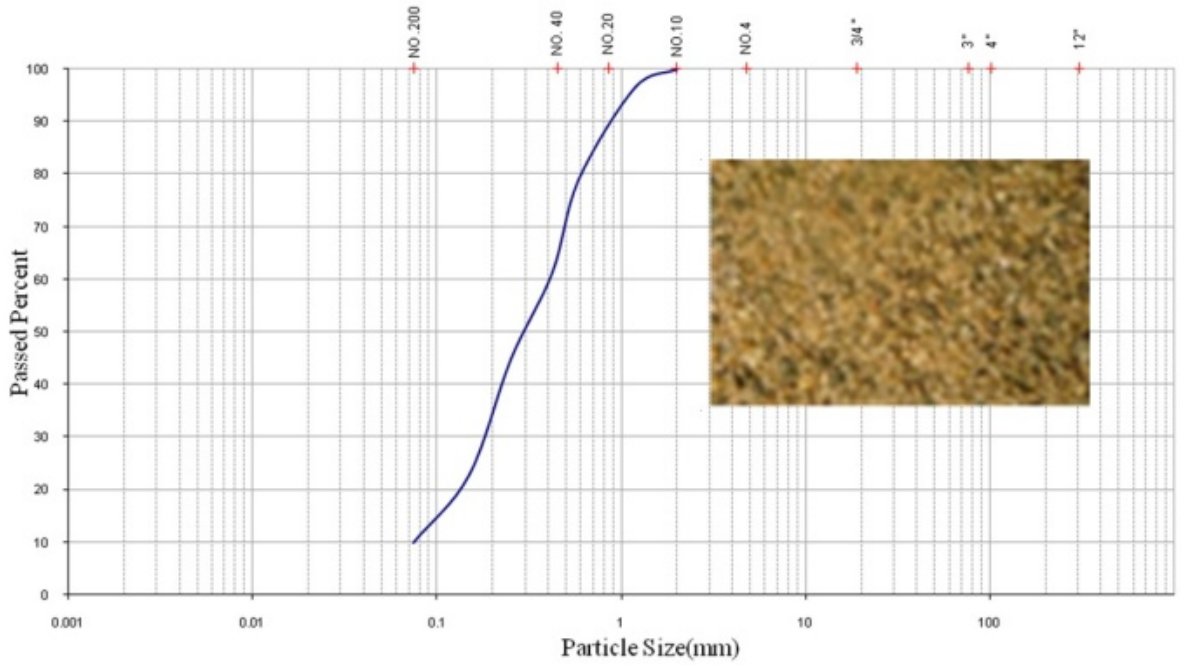

Figure 1. Sand grading curve

https://doi.org/10.17993/3ctic.2023.122.15-58

Table 1. Characteristics of the soil used in the research

γ max	17.35 (kN/m³)	F_c	9.5%
γd max	17.01(kN/m³)	G_s	2.62
γmin	12.88 (kN/m³)	M(moisture)	2 %
γd min	12.63 (kN/m³)	Classification	SP-SM
Dmax	2 mm		

2.2. SPECIFICATIONS OF THE BUILT PHYSICAL MODEL

To physically model the arcing phenomenon, a device was designed and built. Fig. 2 shows the fabricated device and test details. The physical model consists of a metal skeleton, in the upper part of which is a rectangular cube tank with a steel frame with internal dimensions of 400 x 1830 and a height of 1250 mm. Its main skeleton is made of steel plates with a thickness of 10 mm and a stud profile. 200 were made. In the outer part of the side plates, five rows of 80-grade corner type hardeners have been used. To increase the strength, the two parts of the skeleton are welded together using 100-grade stud material to eliminate lateral deformation in the skeleton due to the lateral pressure of the soil and the overhead pressure caused by the loading jack. The lower part of the structure consists of three rows of grade 200 stud profiles, along with a 100 mm thick plate welded, and the upper skeleton is made of 100- grade studs with the help of four legs to this 3000 x 600 mm plate is connected. In total, the height of the device is 2200 mm. Two 10 mm thick steel plates are installed on the bottom of the machine's tank, which can be moved to the sides in a sliding manner, and as a result, the distance between the two plates, which is equal to the width of the valve, can be adjusted. Four separate rectangular pieces with widths of 10, 20, 30, and 35 cm were used for movable valves. When using each valve, the two side plates are opened to the sides as wide as the valve, and the desired valve is placed between the two jaws embedded in the side plates, which serve both as a stiffener and as a guide for the valve movement would take. The valve is secured in place using eight provided screws. These valves are made of a 10 mm thick sheet and could move down up to 40 mm. On both sides of the tank, two transparent Plexiglas plates with a thickness of 30 mm were installed to observe the changes in soil locations. To increase the rigidity, a steel grid with stiffeners of 50 mm height and 20 mm thickness was installed, which could be opened, and each of them was connected to the skeleton by 20 screws.

According to Fig. 2, in order to measure the displacements applied to the valves, a strain gauge was installed under the valves. Also, to measure the stresses involved on the valves by the sand, a stress gauge was also established under the device, so that the applied stress from the valves is directly transferred to the stress gauge.

https://doi.org/10.17993/3ctic.2023.122.15-58

To apply displacement to the valve, a 10-ton hydraulic jack with a stroke of 70 mm with the ability to adjust the speed was installed under the stress gauge, which enables displacement be applied to the valves. Also, a 20-ton hydraulic jack with a 50 mm stroke with a rigid pressure plate was designed and built to spread the overhead pressure. This overhead pressure system was able to be installed on the device using a roof crane made for this purpose. This capability provided the possibility of filling the tank by installing the sand precipitation system and then re-installing the loading system.

The dimensions of the tank have been chosen according to the maximum width of the valve and the type of soil used, and other physical models have been designed in such a way that while removing the effect of the side borders (walls of the tank) on the results, it is not too large as required so that It is possible to fill and empty the tank. Researchers have chosen physical models with different dimensions to study the arcing phenomenon. In this research, the criteria considered for the study of underground tunnels have been used to select the size of the tank size. In the model made by Branko and his colleagues, the distance from the center of the tunnel with a diameter of 55 cm to the lateral borders of the model is 1.2 times the diameter of the tunnel. in the model made by Kim and his colleagues, for a tunnel with a diameter of 7 cm, this distance is 7 times The diameter of the tunnel selected. On average, in most of the designed modes, the distance from the side walls to the center of the tunnel is in the range of 4 to 6 times the diameter of the tunnel. In this research, taking into account the recommendations of previous researchers and the difficulties caused by building a physical model with large dimensions as well as filling and emptying the tank for multiple tests, the distance from the side walls to the center of the valve with a maximum width (35 cm) is more than 5 times the width of the valve (exactly 5.22 times) was chosen. The width of the built model is equal to 183 cm and equal to the length of the full Plexiglas sheet.

After designing the initial dimensions of the model, the effect of the distance of the side walls selected for the tank was investigated using a numerical model. In this way, in the built numerical model corresponding to the dimensions of the physical model, the distance of the lateral borders of the model was increased to 1.5 and 2 times the initial value, and the results were compared with the values obtained from the selected state. Based on the results obtained from the numerical model, the stresses and strains created as a result of the occurrence of the arch phenomenon did not change with the increase in the distance of the lateral borders. Therefore the distance of 5 times the width of the valve is acceptable for the lateral boundaries of the model.

In the construction of the physical model, the issue of model rigidity and removal of model deformations should be considered. The physical model should have been designed and built so that it would not show any deformation due to the overhead jack force. This issue is significant, especially in the strain measurement results using the image speed measurement method. For this purpose, the box's design was done with great care, and steel sheets with the required hardeners were used to make the

https://doi.org/10.17993/3ctic.2023.122.15-58

box. To check the rigidity, the designed physical model was also modeled in the Abaqus software environment. The displacements caused by the lateral pressure caused by the soil and the force applied by the overhead jack were calculated. It was found that the amount of horizontal displacement caused by using a uniform pressure of 2 kg/cm2 on the vertical sides of the steel tank and the Plexiglas plate, which is more than the maximum pressure applied to the walls during the tests, is at most 1 mm. In general, the amount of deformations is minimal and can be ignored, and therefore the built physical model has sufficient rigidity against the applied loads. Modeling of the machine body in Abaqus software is shown in Fig. 3.

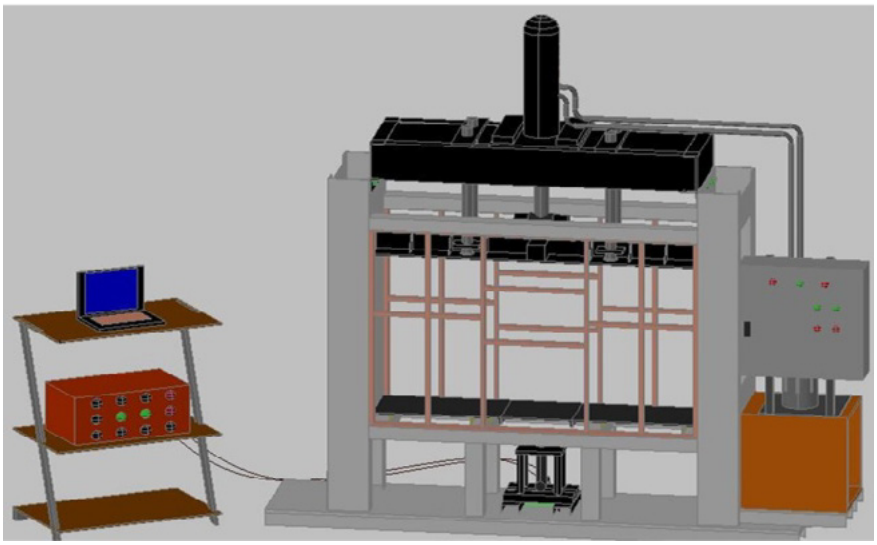

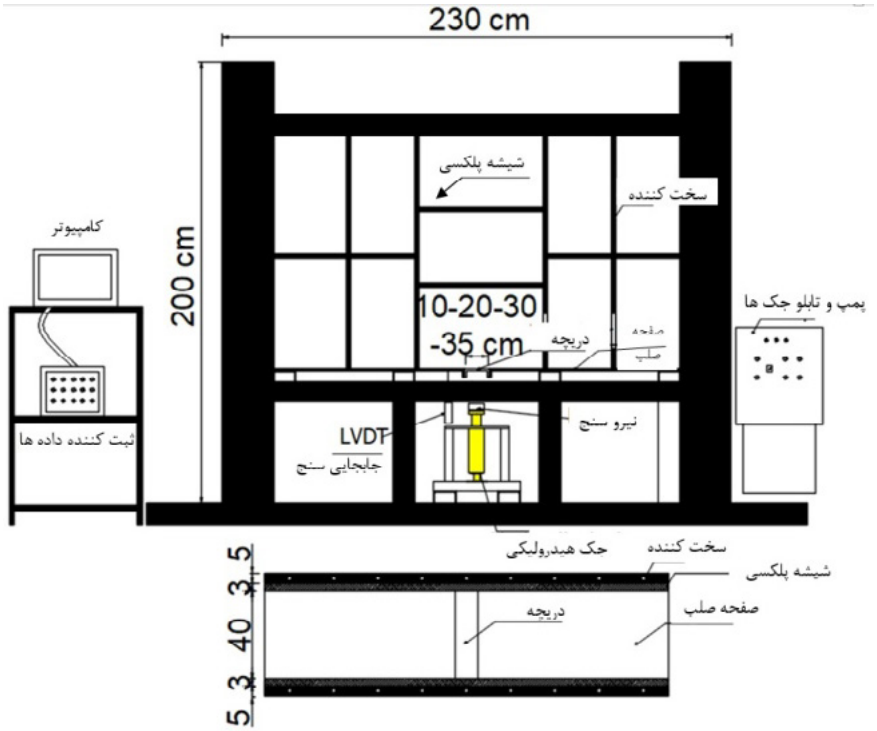

https://doi.org/10.17993/3ctic.2023.122.15-58

Figure 2. Built physical model and used strain gauges

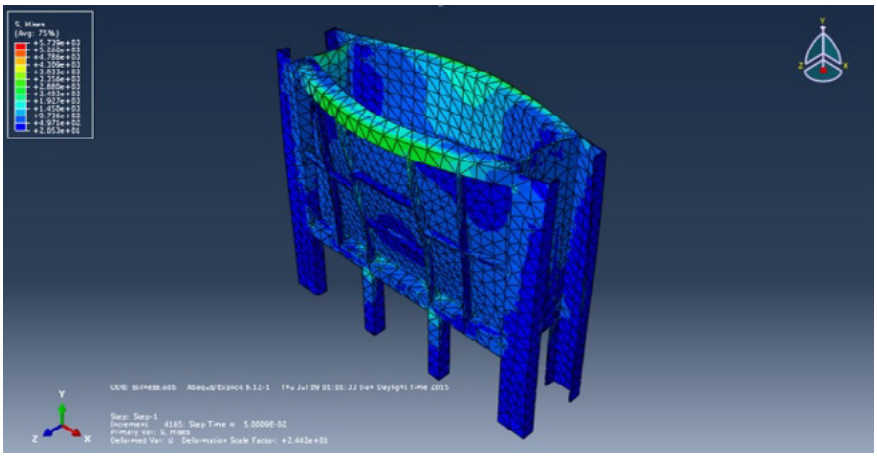

Figure 3. Modeling of the machine body in Abaqus software

https://doi.org/10.17993/3ctic.2023.122.15-58

3. NUMERICAL MODEL

Abaqus software has been used for the numerical modeling of the arcing phenomenon. To choose the appropriate element classification, both element type and mesh density have been investigated. To select the proper element type in the base model, the types of introduced elements were checked. The selection of the proper kind of element is made based on the criteria of producing stress conditions. This means that the elements that can establish the stress conditions in place based on the geotechnical characteristics of the site with the highest accuracy and the lowest computational cost have been selected as the appropriate elements to continue the research. Based on the results obtained from these models and comparing the trends of crown changes with each other, the CPE4 element was selected as the most suitable type of element.

In addition to studying the element type, the effect of meshing density on the results has also been investigated. In this way, for different kinds of elements, different meshing densities were also checked and matched with the values of the in-place stresses. To choose the best density of meshing, triangular and quadrilateral elements with different thicknesses were tested, and the changes in the accuracy of the results and their quality were investigated in different modes. Based on these studies, models with coarser meshing do not have smooth behavior in presenting results, and finer meshing gives smoother results. For example, according to the results of this review and preliminary explanations, CPE4 elements with the meshing shown in Figure 4 were selected as the most suitable mode in the model.

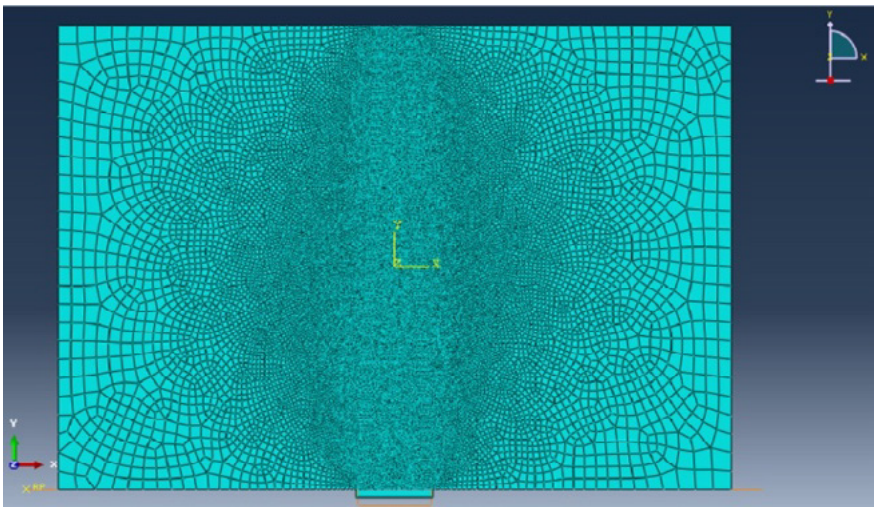

Figure 4. Selected elements in the numerical model

3.1. BEHAVIORAL MODEL GOVERNING THE ARCING PHENOMENON

The behavior before yielding is defined as linear elastic with the secant shear modulus as follows:

https://doi.org/10.17993/3ctic.2023.122.15-58

$$Gs = \frac{\tau_y}{\gamma_y} \quad (1)$$

Where and are the strain and shear stress at the yield point, respectively, which can be obtained directly from the test data (the shear stress corresponding to calculating, the thickness of the shear zone must be assumed. Before the formation of the shear band, the shear strain can be seen to have an almost uniform distribution throughout the height of the specimen (D). As a result, it can be defined as follows:

$$\gamma_y = \frac{\delta\chi_y}{D} \quad (2)$$

The same can be considered for the peak shear strain as follows (assuming that the shear band has not yet formed):

$$\gamma_p = \frac{\delta\chi_p}{D} \quad (3)$$

As a result, the plastic shear strain at the peak point will be as follows:

$$\gamma_p^p = \frac{\delta\chi_p - \delta\chi_y}{D} \quad (4)$$

Young's modulus (E) is obtained from the following equation:

$$E = \frac{9KG_s}{3K + G_s} \quad (5)$$

Where K is the bulk modulus. Both the bulk modulus (K) and the secant shear modulus (G_s) are dependent on the stress level, and to consider this dependence, the following equations have been used:

$$K = K_0 \left(\frac{P}{P_{ref}} \right)^b \quad (6)$$

$$G_s = G_0 \left(\frac{P}{P_{ref}} \right)^b \quad (7)$$

Where P_{ref} is the reference pressure for which and Pressure power (b) is a component that expresses the change of elastic module with isotropic pressure. The value of b ranges from 0.435 in small strains to 0.765 in large strains according to the research of Root et al. The appropriate value for the b parameter to show the increase in shear hardness depending on the stress level is 0.5.

Poisson's ratio can be defined using the following equation :

https://doi.org/10.17993/3ctic.2023.122.15-58

$$v = \frac{3K - 2G_s}{2\left(3K + G_s\right)} \tag{8}$$

In Figs. 5 and 6, respectively, the diagrams of changes in bulk modulus and modulus of elasticity against the shift in average effective stress are presented.

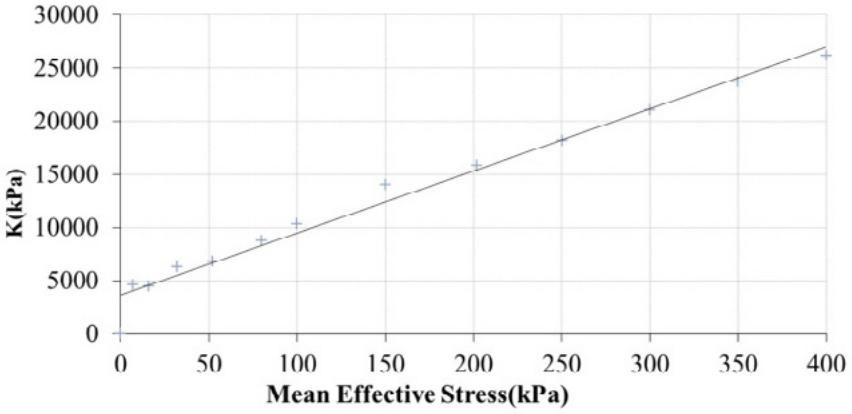

Figure 5. Diagram of bulk modulus against average effective stress

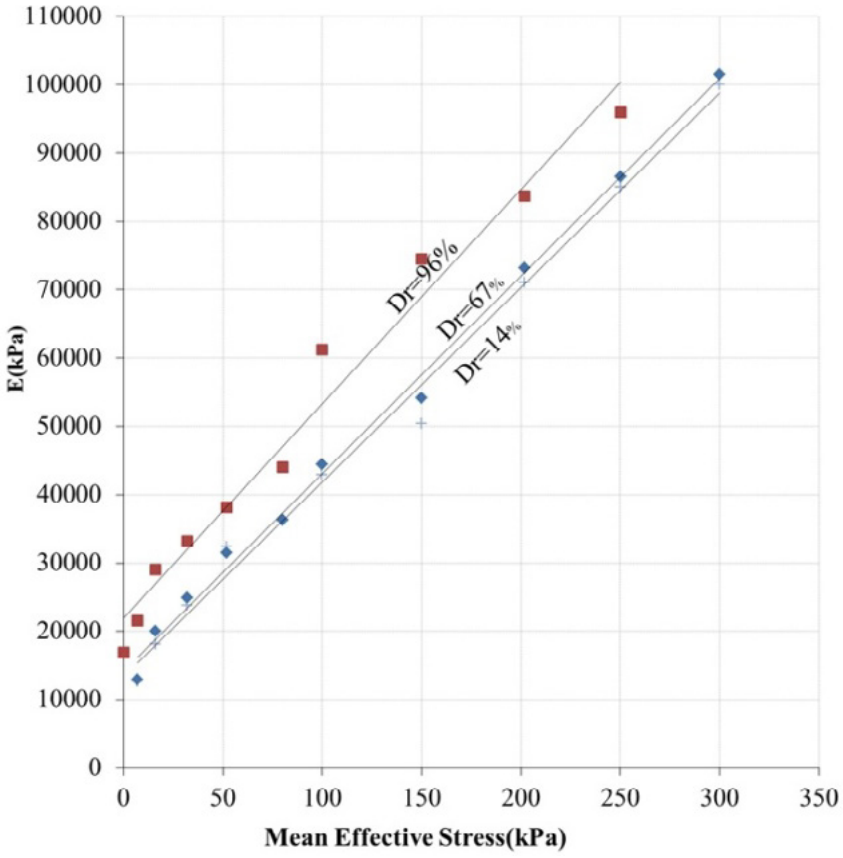

Figure 6. Diagram of modulus of elasticity - average effective stress

https://doi.org/10.17993/3ctic.2023.122.15-58

3.2. RUPTURE COVER

In this research, the behavior model used for sand is the elastoplastic behavior model with the Mohr-Coulomb rupture criterion. The hardening and softening behavior dependent on isotropic strain is considered, and to apply this behavior model to the quiet finite element environment ABAQUS 2012 software is coded in FORTRAN language and introduced in ABAQUS software using Visual Studio compiler.

3.3. FRICTION HARDENING

Vermeer and de Borst proposed the equation (9) for the friction-hardening behavior of geotechnical materials, in which the mobilized friction angle (φ_m) depends on the plastic strain (γ_p) and gradually increases until it reaches the peak friction angle:

$$\operatorname{Sin}\varphi_m = 2\left(\frac{\sqrt{\gamma_p \times \gamma_p^p}}{\gamma_p + \gamma_p^p}\right)\operatorname{Sin}\varphi_p \tag{9}$$

Where γ_p^p the plastic shear strain at the peak friction angle is φ_p.

The equation (10) for the variable expansion angle is presented by Rowe, which is called the stress expansion equation and is as follows:

$$\operatorname{Sin}\Psi_m = \frac{\sin\varphi_m - \sin\varphi_{cr}}{1 - \sin\varphi_m \sin\varphi_{cr}} \tag{10}$$

$$\operatorname{Sin}\varphi_{cr} = \frac{\sin\varphi_p - \sin\Psi_p}{1 - \sin\varphi_p \sin\Psi_p} \tag{11}$$

Where Ψ_m and φ_m are the mobilized expansion angle and the mobilized friction angle, respectively, φ_{cr} is the critical friction angle or constant volume friction angle. The mobilized expansion angle is initially hostile and increases with the increase of plastic strain. To avoid this considerable negative value of the expansion angle in minor strains, the following equation was presented by Surid et al.

$$\operatorname{Sin}\Psi'_m = \sin\Psi_m\left(\frac{\sin\varphi_m}{\sin\varphi_{cr}}\right)^p \tag{12}$$

Power P controls the shape of the mobilized expansion angle and is considered 1 in this study. The change in the mobilized expansion angle with plastic strain is shown in Figure 7 for different values of P power.

https://doi.org/10.17993/3ctic.2023.122.15-58

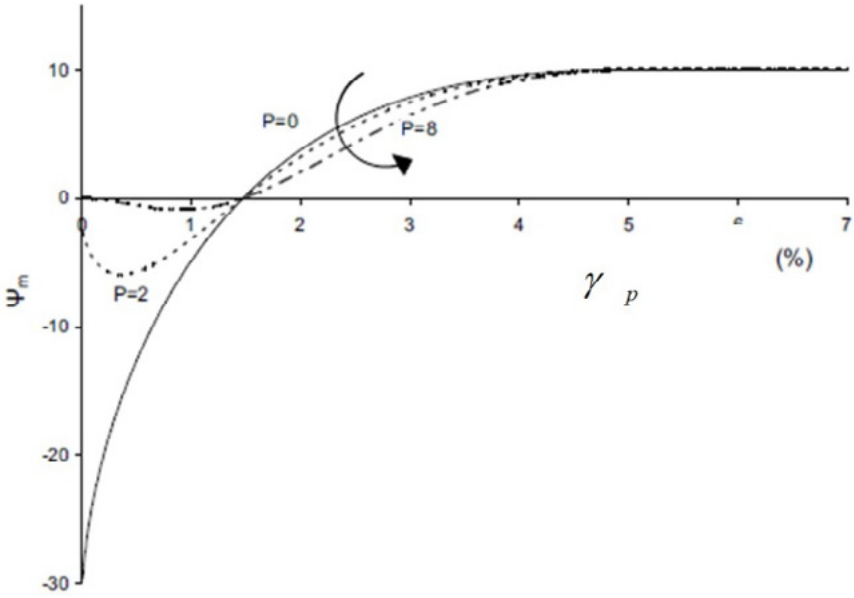

Figure 7. Change of the mobilized expansion angle with P power

3.4. FRICTIONAL SOFTENING

In the two-block shear model of Shibuya et al., it is assumed that after the formation of the shear band (just after the peak point), all plastic shear deformation is formed within the shear band, while the rest of the soil mass remains elastic. Stays assuming that the shear band width (d_B) is $16d_{50}$, where d_{50} is the average sand particle size, the plastic shear strain at which softening is complete (γ_f^p) will be:

$$\gamma_f^p = \gamma_p^p + \frac{\delta\chi_p^p - \delta\chi_y}{16d_{50}} = \frac{\delta\chi_p^p - \delta\chi_y}{D} + \frac{\delta\chi_p^p - \delta\chi_y}{16d_{50}} \qquad (13)$$

The strain-dependent softening with the decrease of the mobilized friction angle φ_m and the mobilized expansion angle Ψ_m with the increase of the plastic shear strain is as follows:

$$\varphi_m = \begin{bmatrix} \varphi_p - \frac{\varphi_p - \varphi_{cr}}{\gamma_s^p}\gamma_{oct}^p & \text{for} & \gamma_p^p \le \gamma_{oct}^p < \gamma_f^p \\ \varphi_{cr} & \text{for} & \gamma_{oct}^p > \gamma_f^p \end{bmatrix} \qquad (14)$$

$$\Psi_m = \begin{bmatrix} \Psi_p\left(1 - \frac{\gamma_{oct}^p}{\gamma_s^p}\right) & \text{for} & \gamma_p^p \le \gamma_{oct}^p < \gamma_f^p \\ \Psi_{cr} & \text{for} & \gamma_{oct}^p > \gamma_f^p \end{bmatrix} \qquad (15)$$

$$\gamma_{oct}^p = \frac{2}{3}\left[\left(\varepsilon_1^p - \varepsilon_2^p\right)^2 + \left(\varepsilon_2^p - \varepsilon_3^p\right)^2 + \left(\varepsilon_3^p - \varepsilon_1^p\right)^2\right]^{1/2} \qquad (16)$$

https://doi.org/10.17993/3ctic.2023.122.15-58

Where φ_p and φ_{cr} are the peak friction angle and critical friction angle, respectively, Ψ_p is the peak expansion angle and the plastic shear strain at the end of softening. Also, plastic strains are the main ones.

3.5. THE DEPENDENCE OF THE FRICTION ANGLE AND EXPANSION ON THE STRESS LEVEL

Since the fact that the friction and expansion angles are dependent on the stress level, and this fact has also been observed in laboratory tests, to determine the shear strength components of sand corresponding to the stress level, direct shear tests under different stress levels were performed. In a particular soil, the value of the internal friction angle φ depends on the amount of stress applied to it. The lower the normal stress, the greater the internal friction angle φ. According to the theory of stress-expansion ratio, the amount of porosity, moisture and expansion are as necessary as the effective normal and shear stresses in analyzing the results and soil behavior. The stress-expansion ratio equation is presented as follows:

$$\frac{\tau}{\sigma} = \tan\left(\varphi_{cr} + \Psi\right) \tag{17}$$

In the above equation, the expansion angle Ψ depends on the initial conditions of the soil. In this research, the results obtained from the experiments have been modified based on the theory of the stress-expansion ratio.

The relationship between the peak friction angle and the critical friction angle can be approximated by the following equation:

$$\tan\varphi_p = \tan\varphi_{cr} + \alpha\,\tan\psi_p \tag{18}$$

Where α is a constant value, Shibuya and his colleagues have shown that simple shear behavior in the soil is only possible within the range of the shear band. In the box of a simple straight cutting machine (no rotation of the loading plate, smooth walls, adjustable distance between the upper and lower metal plates equal to the thickness of the cutting strip), α can be considered equal to 1. The peak friction angle in-plane strain can be calculated as follows:

$$\mathrm{Sin}\,\varphi_p = \frac{\tan\varphi_p}{\sin\Psi_p + \sin\Psi_p\tan\varphi_p} \tag{19}$$

Figure 8 Changes in stress ratio and volume change (obtained through the vertical displacement δ_y of the upper metal plate) with the horizontal displacement δ_x in the direct shear test on "Toyura sand" in a dense state (based on the data of Shibuya et al.) is showing. According to Figure 8, soil behavior can be divided into 4 distinct parts:

https://doi.org/10.17993/3ctic.2023.122.15-58

Quasi-elastic behavior (OA): Up to point A, the soil deforms quasi-elastically. The nonlinear behavior of the soil without any expansion is observed. δ_{xy} is the horizontal displacement at $\delta_y/\delta_x = 0$.

Hardening behavior (AB): From points A to B, the soil "yields" (enters the plastic zone) and expands. Point B corresponds to the peak shear stress and shows the hardening behavior of the soil. δ_{xp} is the horizontal displacement at $\delta_y/\delta_x = 0$.

Softening behavior (BC): From points B to C, the soil experiences softening behavior. Just after the peak point, a horizontal shear band extends through the middle of the sample. Softening is completed at point C. δ_{xf} is the horizontal displacement at $\delta_y/\delta_x = 0$.

Residual behavior (CD): shear accumulates along the entire length of the shear band.

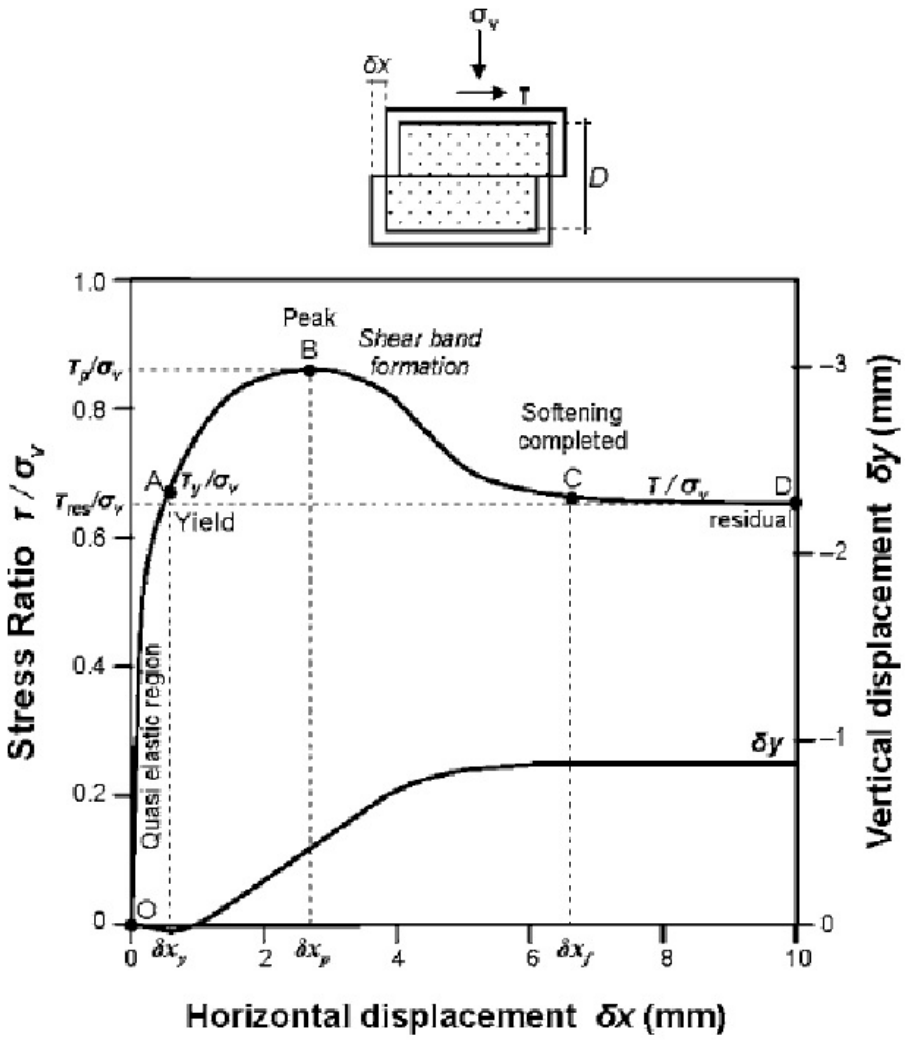

Figure 8. Changes in the ratio of stress and volume with horizontal displacement in the cutting test on Toyoura sand

https://doi.org/10.17993/3ctic.2023.122.15-58

3.6. THE PARAMETERS OF THE BEHAVIORAL MODEL OBTAINED FROM THE EXPERIMENTS

The characteristics of the sand used in the research, such as modulus of elasticity, friction angle, and expansion angle, were extracted from the results of direct and triaxial cutting tests. In Tables 2-4, the properties of sand for three different relative densities of loose, medium, and dense are shown. In these tables, y_d, σn, τp, and τcr are dry density, applied normal stress, maximum shear stress, and critical shear stress, respectively. Also, φ_p, φ_{cr}, and Ψ are the peak friction angle, critical friction angle, and expansion angle, respectively, which were obtained directly from the results of the experiments. φ_{cor} is the corrected friction angle obtained from Equation (18) using Ψ and φ_{cr}. φ_{pl} is the plane strain friction angle used in the simulation and is obtained from Equation (19). δ_{xy}, δ_{xp}, and δ_{xf} are the horizontal displacements of the shear box at the yield, peak, and critical points, and the strains corresponding to yield points are peak and critical. For example, the diagrams related to the behavioral model and the changes in the internal friction angle and the expansion angle with plastic strain for a relative density of 25% are presented in Figures 9 to 11.

Table 2. Material properties from experimental tests for dense sand (Dr=92%).

No	Dr	Ψ	φcor (corrected)	φpl (plane strain)	γ_y	γ_p	γ_f
1	92	6.27	47.80	57.36	0.00	0.10	0.27
2	92	5.03	44.70	53.65	0.00	0.11	0.21
3	92	4.81	36.89	44.26	0.00	0.11	0.26
4	92	4.80	41.15	49.38	0.00	0.11	0.27
5	92	4.74	46.28	55.53	0.01	0.11	0.27
6	92	4.54	41.48	49.78	0.01	0.12	0.24
7	92	4.56	36.52	43.83	0.01	0.10	0.26
8	92	4.45	36.25	43.50	0.01	0.16	0.26
9	92	4.36	35.53	42.63	0.01	0.13	0.26
10	92	3.59	34.56	41.41	0.01	0.16	0.24

https://doi.org/10.17993/3ctic.2023.122.15-58

Table 3. Material properties from experimental tests for sand with medium density (Dr=68%).

No	Dr	Ψ	φcor (corrected)	φpl (plane strain)	γ_y	γ_p	γ_f
1	68	6.92	45.45	54.55	0.00	0.26	0.35
2	68	6.63	45.20	54.24	0.00	0.22	0.28
3	68	5.47	42.00	50.40	0.00	0.16	0.24
4	68	4.04	43.83	52.60	0.00	0.14	0.22
5	68	3.85	43.86	52.63	0.01	0.16	0.29
6	68	3.01	36.87	44.24	0.01	0.11	0.27
7	68	2.53	41.04	49.25	0.01	0.15	0.24
8	68	2.04	39.31	47.18	0.01	0.14	0.32
9	68	1.74	39.81	47.77	0.01	0.14	0.28
10	68	0.70	38.51	46.22	0.01	0.14	0.22

Table 4. Material properties from experimental tests for loose sand (Dr=25%).

No	Dr	Ψ	φcor (corrected)	φpl (plane strain)	γ_y	γ_p	γ_f
1	25	8.87	40.07	48.09	0.00	0.22	0.30
2	25	7.41	35.13	40.54	0.00	0.24	0.29
3	25	7.33	34.08	38.87	0.00	0.21	0.31
4	25	4.22	30.60	34.63	0.00	0.17	0.27
5	25	2.47	38.97	51.48	0.01	0.22	0.29
6	25	1.81	35.71	44.69	0.01	0.17	0.29
7	25	1.05	34.61	42.97	0.01	0.19	0.32
8	25	0.51	33.93	41.97	0.01	0.17	0.31
9	25	0.82	33.05	40.14	0.01	0.27	0.32
10	25	0.10	32.17	38.93	0.01	0.32	0.42

https://doi.org/10.17993/3ctic.2023.122.15-58

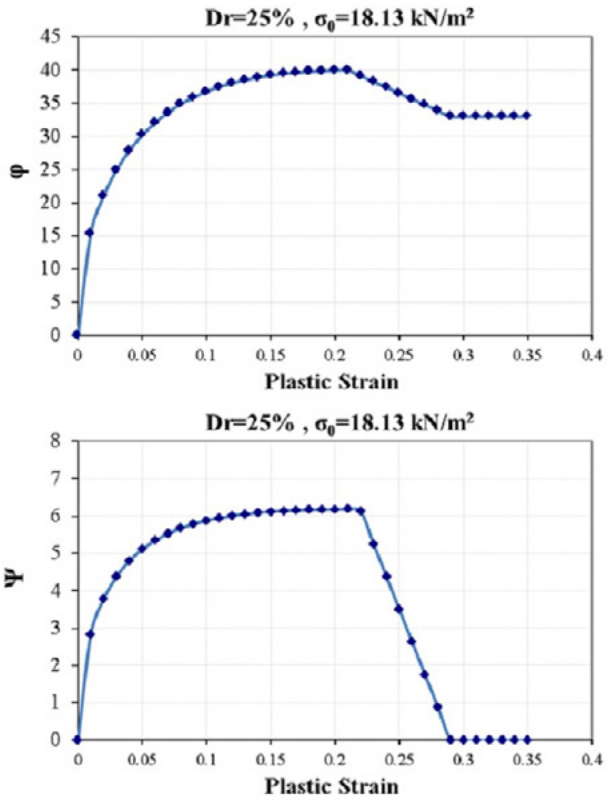

Figure 9. Changes of internal friction angle and expansion angle for relatively loose sand with low head load. (Dr=25%, ɕn=18.13KN/m3)

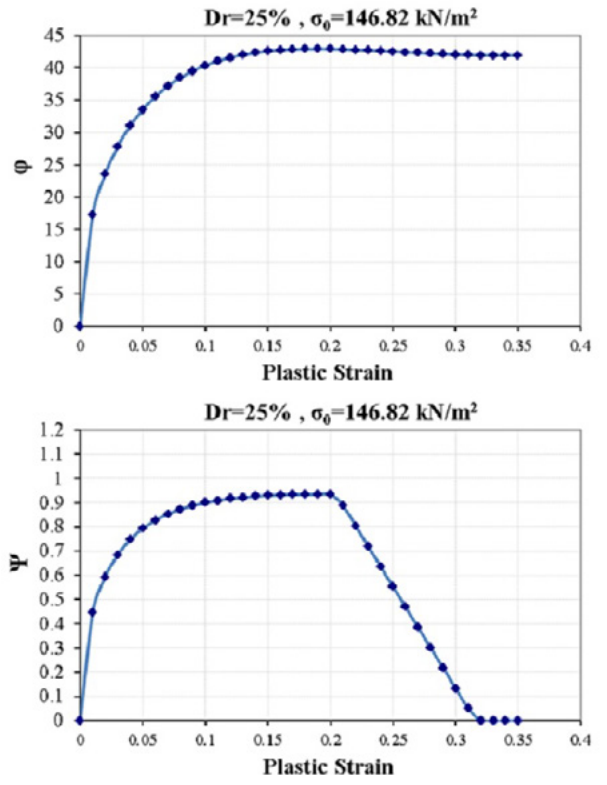

Figure 10. Changes of internal friction angle and expansion angle for relatively loose sand with medium overhead. (Dr=25%, ɕn=146.82KN/m3)

https://doi.org/10.17993/3ctic.2023.122.15-58

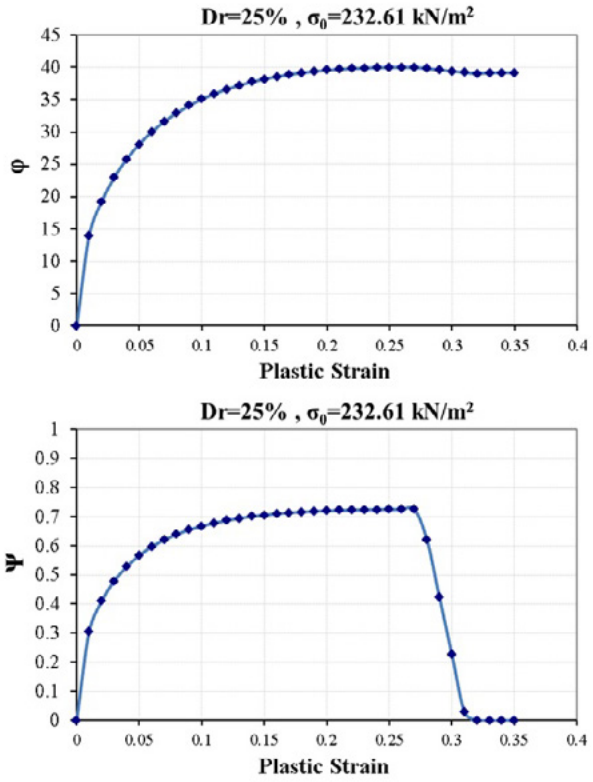

Figure 11. Changes of internal friction angle and expansion angle for relatively loose sand with high overhead. (Dr=25%, σn=232.61KN/m3)

3.7. CALIBRATION OF THE BEHAVIORAL MODEL

To calibrate the presented behavioral model, the direct cutting test was simulated in Abaqus software, and the obtained results were compared with the data obtained from the tests. In the simulation of the direct shear test, due to the lack of change in the stress level during a trial, the elastic modulus is defined as a constant value during the analysis, Still, in the simulation of different tests, the elastic modulus is changed based on the normal stress level. The finite element model and plastic strain gauge are shown in Fig. 12. As an example, Fig. 13 shows the graphs of shear stress and horizontal displacement as well as the vertical displacement and horizontal displacement in experimental tests and numerical modeling under different normal stresses for a relative density of 95%. The comparison between simulated and experimental curves shows their agreement. Therefore, the strain-dependent hardening-softening model should be used in simulating the behavior of granular soils in conditions where deformations are similar to direct shear tests.

https://doi.org/10.17993/3ctic.2023.122.15-58

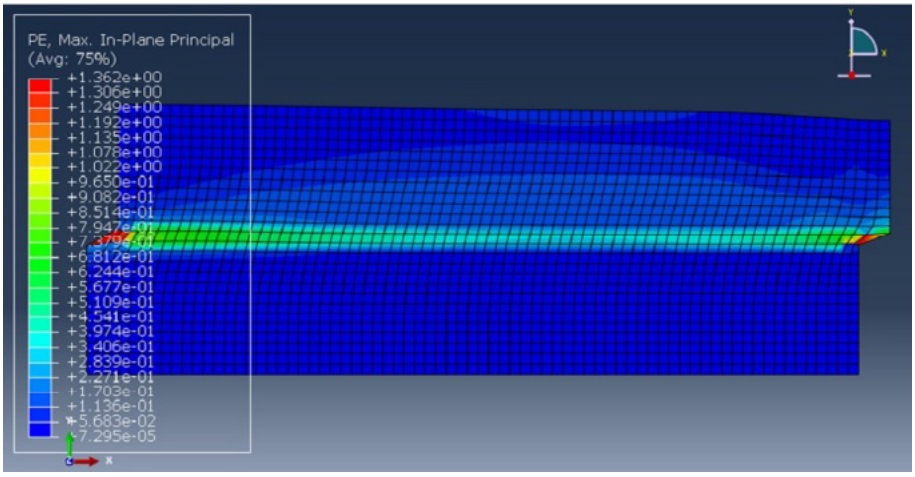

Figure 12. Meshing and plastic strain counters in the numerical model of direct cutting

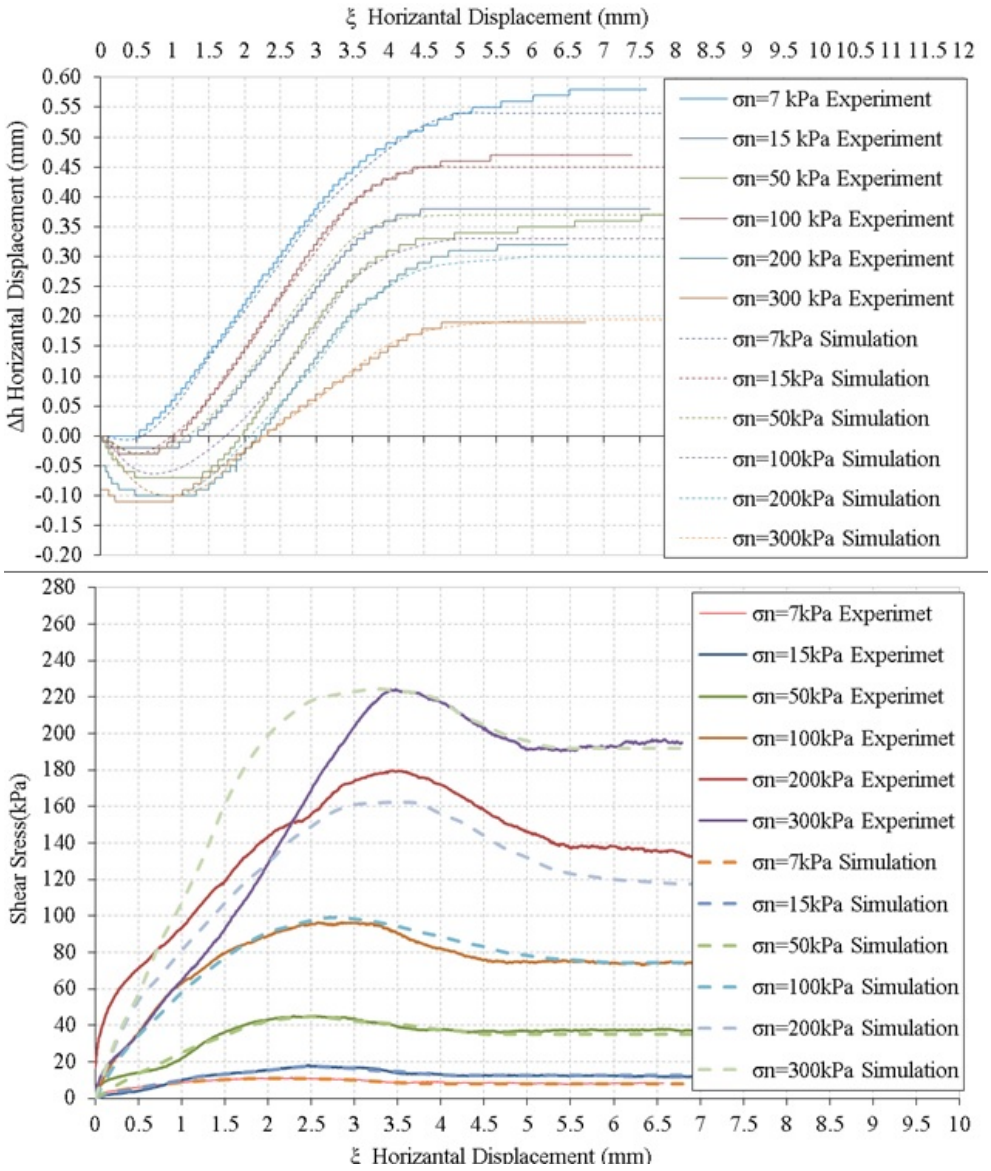

Figure 13. Comparison between shear stress-horizontal displacement and vertical displacement-horizontal displacement in the experiment and numerical results for dense sand (Dr=95%)

https://doi.org/10.17993/3ctic.2023.122.15-58

3.8. NUMERICAL MODEL OF ARC PHENOMENON AND MODELING ASSUMPTIONS

Numerical modeling of the arcing phenomenon has been done in Abaqus software, 2012 edition. The numerical model was created in the graphical environment of the software in such a way that it accurately evokes the laboratory conditions. This numerical model includes three separate parts of the soil mass, tank, and valve, which are mounted together in the Assembly section of the software. The lateral boundaries include supports with degrees of freedom in the vertical direction, and the bottom part of the soil rests on the defined tank. The interaction between different elements is modeled according to actual conditions. In this way, the interaction between the tank and the soil is frictional for sliding movement and hard contact for motion perpendicular to the plane. The coefficient of sliding friction between the tank and the soil is considered equal to 0.3. This number is obtained from the tensile test of the painted metal plate buried in the test sand. A measurement of the rigid contact type leads to the soil elements not passing through the tank elements. Such an interaction is also considered for the soil and valve interaction. To remove the stress concentration in the sharp corner after lowering the valve, the sharpness of this part of the tank has been removed with the help of bending with a minimal radius.

Among the basic cases in modeling the phenomenon of arcing of elements, especially in the areas around the valve. The large size of the components leads to the occurrence of errors in the analysis and the failure of the flow phenomenon during the event of the arcing phenomenon, at the same time, the smallness of the elements also leads to the bulkiness of the analysis and the excessive increase of the analysis time. Therefore, choosing the right size for the details requires trial and error and comparing the results. Of course, the meshing was done according to the capabilities of the software in such a way that the size of the elements around the valve and places with higher strain is smaller and gradually towards the boundaries of the model, with a lower strain rate, the size of the elements increases.

The analysis has been done in two stages, which can be defined in the Step section of the software:

1. The stage of establishing the initial stress is defined as Geostatic in the model.

2. The opening stage of the valve and the beginning of the arcing phenomenon.

In the Abaqus software, it is impossible to define the modulus of elasticity and variable friction angle directly in the graphic part. Of course, the elasticity modulus depending on the stress level, can be determined through the Edit Keywords module. To apply frictional hardening and softening depending on the plastic strain, a program was written in FORTRAN space. This program is compiled through the Visual Studio interface and used in ABAQUS software. In this way, the variable internal friction angle and dependent on plastic strain can be defined in the software. Figs. 14 and 15, respectively show the numerical model along with the boundary conditions and the

https://doi.org/10.17993/3ctic.2023.122.15-58

valve along with the reservoir defined with the curvature applied to reduce the stress concentration.

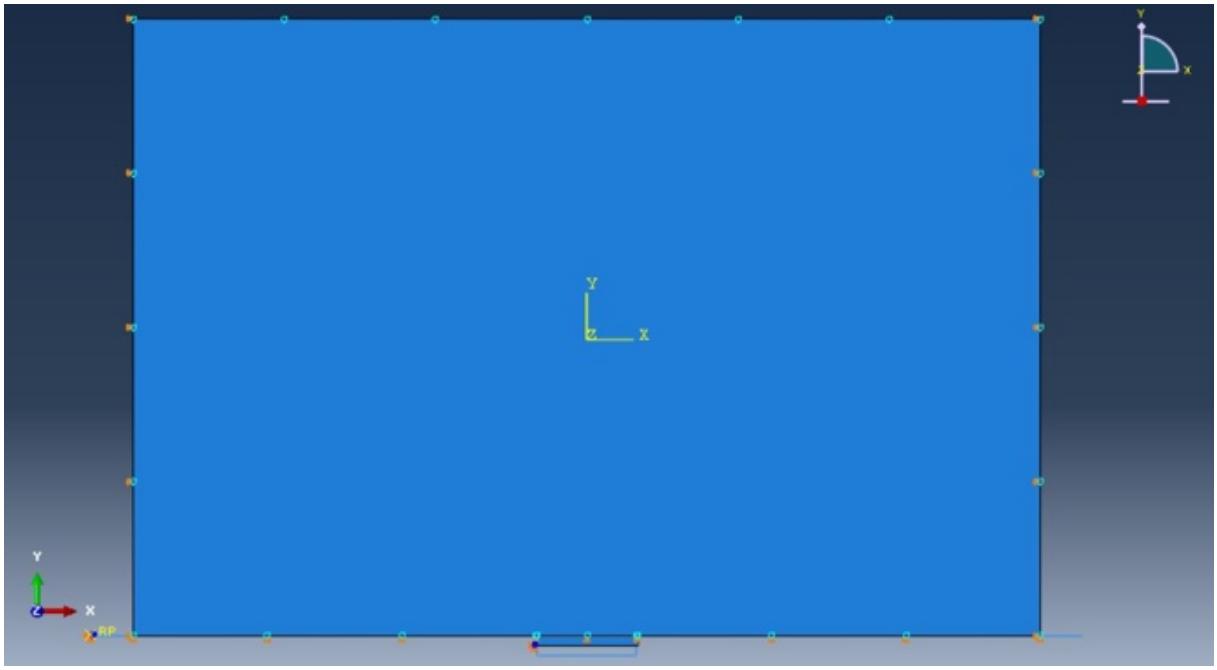

Figure 14. Numerical model and boundary conditions

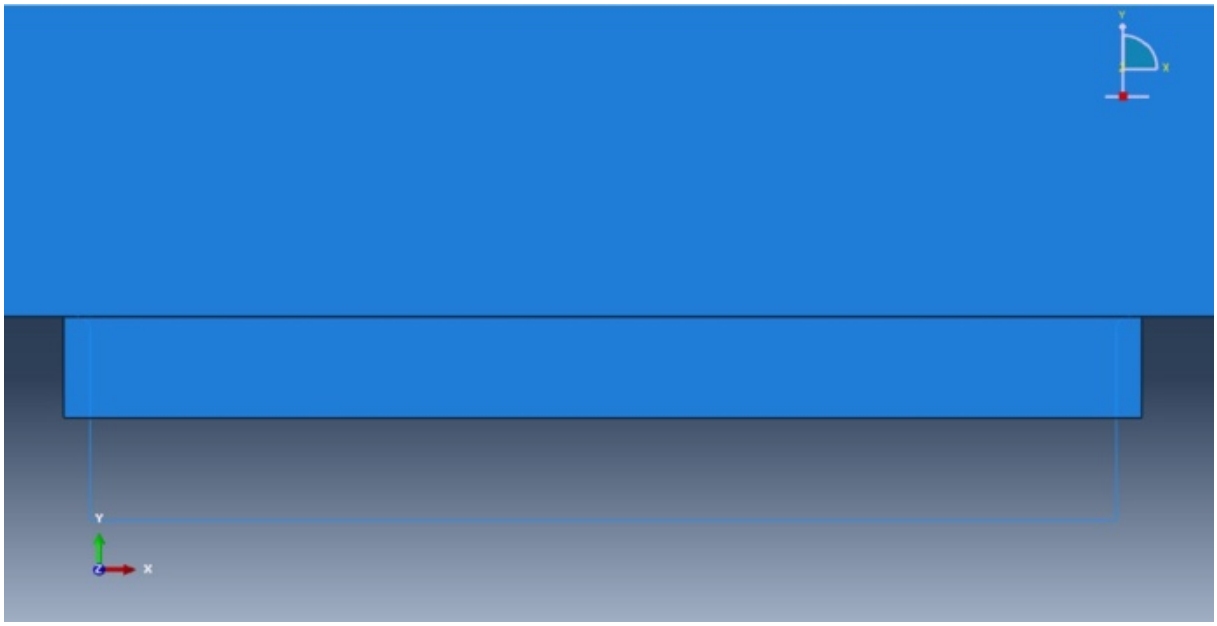

Figure 15. Numerical model and valve modeling details

3.9. ELIMINATING THE EFFECT OF THE ARC IN THE PLACE OF STRESS GAUGES

The research conducted on strain gauges and sensors installed in dams and roads shows an arc effect in their readings, which should be considered in the data used. Islam and his colleagues, in 2014, with finite element analysis and modeling of the

https://doi.org/10.17993/3ctic.2023.122.15-58

strain gauge installed on the road, estimated the amount of arc effect in the strain gauge reading from 2.21 to 2.72 percent. In this research, by using two strain gauges installed in the middle part of the tank and comparing the initial stresses shown by the strain gauges with the calculated stress, the value of the arcing effect was obtained in about 2.5 to 2.8 percent, and the reading data has been modified accordingly.

4. EXPERIMENTS CONDUCTED ON THE PHYSICAL MODEL

Table 5 summarizes the conditions governing the experiments and the results obtained. In the first column of the table (Test No.), the number of the test is inserted in the order it was performed. In the second column (Trapdoor width), the width of the valve used in the experiment is shown. In the third and fourth columns (γ, γd), the amount of wet and dry density of sand in terms of kilonewtons per cubic meter is included in each test. In the fifth column, the relative density (Dr), and the sixth column (σ0), the value of the initial stress applied to the valve without any displacement to the valve or strain in the sand, i.e., γh where γ is the density of the sand and h is the height of the sand to its surface. In the eighth column (σmin), the value of the minimum stress applied to the valve, which was read on the strain gauge during the test, is entered. In the ninth column (Surcharge Pressure), the amount of overhead applied in different tests is presented.

In the following, the results obtained from the experiments are presented as graphs. In these diagrams, the stress applied to the valve, is measured in kilonewtons, is read from the strain gauge installed under the valves and plotted against the displacement of the valve. Because the graph in the direction of ΔH was very long and it was not possible to reach a conceptual and understandable diagram, therefore a logarithmic scale was used in the direction of ΔH. Also, in the direction of ΔH, the numbers read from the chart should be divided by 100 to get the actual displacement of the valve in millimeters.

https://doi.org/10.17993/3ctic.2023.122.15-58

Table 5. Specifications governing each experiment and the results obtained

Test NO.	Trapdoor Diameter	γ (kN/m³)	γ_d (kN/m³)	Dr (%)	σ_0 (kpa)	Surcharge Pressure (kN/m²)
1	10	13.80	13.16	25	8.23	---
2	10	15.60	12.75	68	7.95	---
3	10	16.90	14.21	92	8.88	---
4	20	13.80	14.88	25	8.01	---
5	20	15.60	14.88	68	9.3	---
6	20	16.90	12.75	92	8.01	---
7	30	13.80	12.83	25	8.01	--
8	30	15.60	14.88	68	9.35	---
9	30	16.90	14.97	92	9.35	---
10	35	13.80	12.7	25	9.35	---
11	35	15.60	13.68	68	8.54	---
12	35	16.90	13.68	92	8.54	---
13	35	15.60	14.02	68	8.76	128
14	35	15.60	14.09	68	8.8	212

4.1. THE RESULTS OF THE DATA OF THE STRESS GAUGE INSTALLED ON THE VALVE AND IN THE MIDDLE OF IT (S1).

In Fig. 16, the results of the tests performed in three relative densities of 25%, 68%, and 92% for the valve with a width of 10 cm are presented. As can be seen, after the start of valve movement, the stress immediately drops to about 4% of the initial stress. This minimum stress occurs when the valve moves about 0.06 mm. Then, as the valve continues to move, the tension is constant, and when the valve moves about 1 mm, the tension increases up to 6% of the initial tension and remains almost constant. With the change of the relative density, this stress ratio has changed, so the stress ratio is the highest in the relative density of 25% and the lowest in the relative density of 92%. In this case, it can be said that a stable arc is formed in all tests.

https://doi.org/10.17993/3ctic.2023.122.15-58

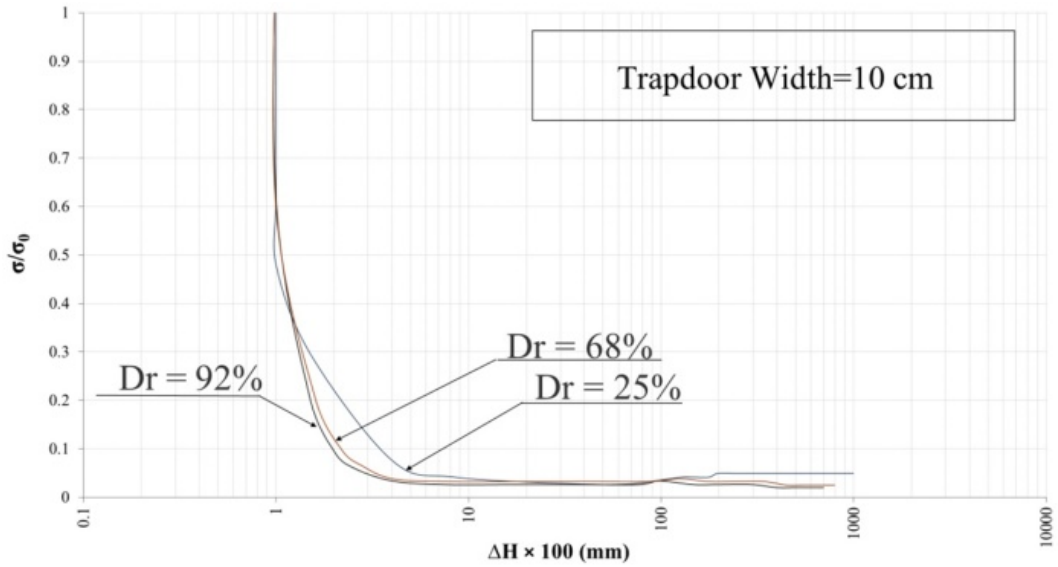

Figure16. Stress diagram in the middle of the 10 cm valve against the change in valve location

In all the graphs, the stress value has decreased sharply at low strains, and after reaching a minimum value, it has taken an upward trend. The minimum amount of stress applied to the valve occurred in the displacement of 0.02 to 0.3 mm of the valve.

As it is clear from these diagrams, four distinct phases can be distinguished in the arc phenomenon:

The first phase: This phase starts immediately after the start of the valve drop, so that the tension applied to the valve is immediately and strongly reduced and reaches the minimum value. In this phase, the soil behaves elastically, and the deformations are small, while the stress changes are huge. At the beginning and before moving the valve, the shear stress values in the sand mass and around the valve are zero, and the principal stresses are vertical and horizontal. As the valve begins to move around the arch area, the shear stress starts to increase, and as a result, the principal stresses deviate from the vertical and horizontal state and rotate. In fact, in this phase, in arc development, the principal stress plane turns by creating shear stresses. So that the value of the principal stresses is reduced to the minimum and the principal stresses are increased to the maximum. In other words, the diameter of Mohr's circle increases in the arched area. This process of changes in the plane of principal stresses continues until the formation of a stable arch.

The Second phase: This phase starts after the minimum stress point. This phase occurs in a wide range of valve displacement and the range of development of plastic strains. In the second phase, plastic strains and, finally, warping start from the side of the valve and proceed in the direction perpendicular to the two ends of the valve towards the surface. Convergence or divergence of this development of plastic strains and rupture depends on the density of the soil and the width of the valve, which determines the stable or unstable arch. In this phase, the phenomenon of flow

https://doi.org/10.17993/3ctic.2023.122.15-58

occurs in the soil mass, so that despite high strains, there is no significant change in the applied stress on the valve.

The third phase: This phase begins with an increase in the applied tension on the valve. At this stage, the separation and formation of a stable arc take place. If there is no stable arc, the rising trend of tension continues.

The fourth phase: In this phase, the total weight of the stable arc is applied to the tension gauge, and the applied tension on the valve remains almost constant. In case of an unstable arc in this phase, the tension will be steady and increasing.

These separate phases are presented in Fig. 17 .

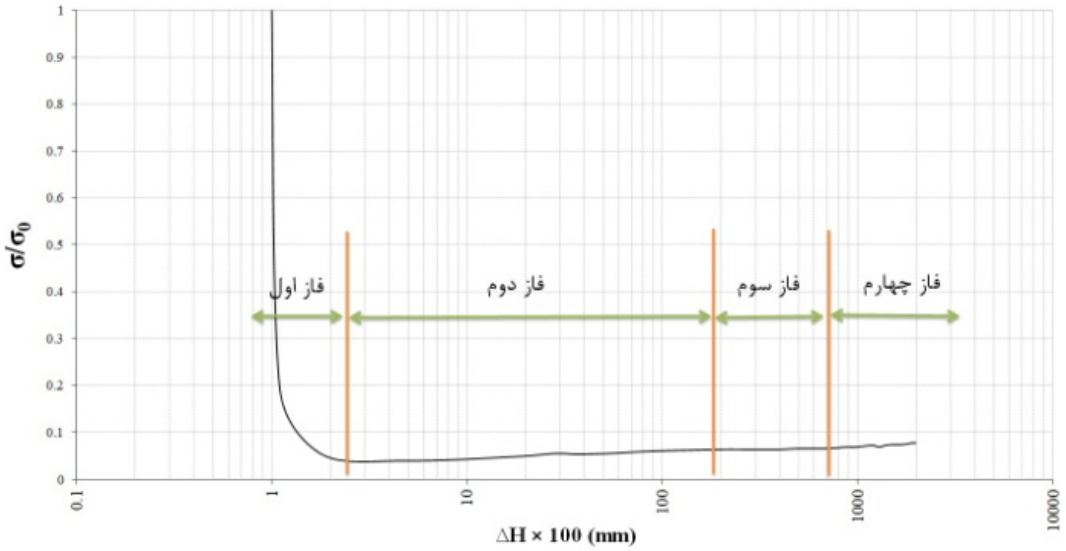

Figure 17. Four distinct phases of stress changes

4.2. COMPARISON OF THE LABORATORY RESULTS WITH THE NUMERICAL MODEL, TAKING INTO ACCOUNT THE DATA OF THE STRESS GAUGE INSTALLED ON THE VALVE AND IN THE MIDDLE OF IT.

The S16 strain gauge was installed in the middle of the valve and recorded the changes in tension during the movement of the valve. To compare the results obtained from the physical model and numerical modeling, the results have been drawn in a single diagram for the stress applied in the middle of the valve. In the numerical model, the element, such as the location of the stress gauge S16, is selected, and its results are presented. Fig. 18 shows an example of graphs obtained from laboratory data and numerical analysis results for a valve with a width of 10 cm and a relative density of 25%. As can be seen, the trend of changes in stress ratio with valve drop in both graphs obtained from experiments and numerical analysis is almost the same. Of course, there is a small difference of about 5% to 10% between the values of the stress ratios, which is caused by the error of the experiment and numerical analysis. It should be noted that with the increase in relative density, the

https://doi.org/10.17993/3ctic.2023.122.15-58

difference between the results of experiments and numerical analysis has decreased. This is due to the reduction of the error caused by the uniformity of the sand, as well as the more excellent compatibility of the parameters obtained from the direct cutting tests and the arc mechanism. As can be seen, in the diagram related to the numerical model, as well as the physical model, the four regions defined in the previous section can be distinguished. Of course, to reduce the error in low relative densities, the size of the elements was increased so that the dimension of the component is as close as possible to the width of the cutting area. However, this reduced the slope of the elastic region and the rate of displacements and strains, especially in the part of the flow phenomenon. In other valves, the agreement between the results of the experiments in the physical model and the numerical model is evident.

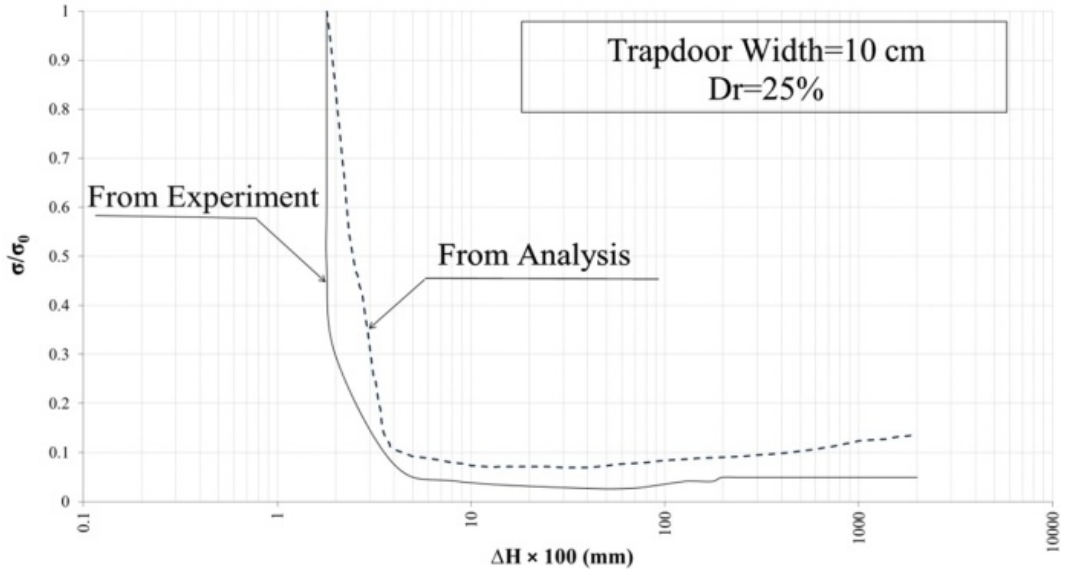

Figure 18. Comparison of the results of the physical model and the numerical model for a valve with a width of 10 cm and a relative density of 25%.

According to these results, it can be seen that by moving the valve downwards, the stress applied on the strain gauge drops drastically, and in the elastic range, this stress drop is very severe. As the valve moves, this drop continues with a gentler slope until it reaches a minimum value and an insignificant number near zero. Of course, this state occurs in a stable arc, and when an unstable arc occurs, the amount of increase in the stress applied to the strain gauge can be seen within the range of 10 mm displacements of the valve. Also, the agreement of the numerical modeling results with the results obtained from the physical model increases with increasing density.

https://doi.org/10.17993/3ctic.2023.122.15-58

4.3. THE RESULTS OBTAINED FROM THE PIV METHOD CONCERNING THE MEASUREMENT OF STRAINS DURING THE OCCURRENCE OF THE ARCING PHENOMENON

The PIV method has been used to measure the strains created during the arcing phenomenon. Fig. 19 shows an example of the results of the analysis of strains during the event of the arch phenomenon for a displacement of 10 mm of the valve. In this image, the upper and left figures are the color counters of the strains, and the upper right figures are the alignment lines of the strains. Also, in the diagram shown, the diagrams related to the strain changes corresponding to the location of stress gauges S18 to S23 (valve sides) are presented. As can be seen, the shear strain meters show a stable arc. Also, in these figures, the graphs related to the strain changes at 5 points where the strain gauge is installed, against the displacement of the valve, show that the relationship between the strain changes and the valve displacement is almost linear. Also, most strains are related to the sides of the valve. In the case of not creating a stable arch, the shape, and development of shear counters are different. Fig. 20 shows the shear strain counters of the unstable arch for a valve with a width of 30 cm and a relative density of 25%. The development of shear strains in this form is initially in the converging direction and towards the formation of a stable arch, still the continuation of the process of moving the valve, the shear strains developed towards the sand surface and led to the instability of the arc. While with the densification of the sand, the rate of formation of a stable arc is higher, and it does not allow the total rupture of the sand mass and a stable arc is formed. The development of shear strains first converged towards the formation of a stable arc, but at the same time, the vertical component of the shear strains developed towards the sand surface and led to the non-formation of a stable arc. Of course, with the densification of the sand, the strains are reduced, and the tendency to converge and form a stable arc is evident. Also, with the densification of sand, the growth rate of shear strains decreases.

https://doi.org/10.17993/3ctic.2023.122.15-58

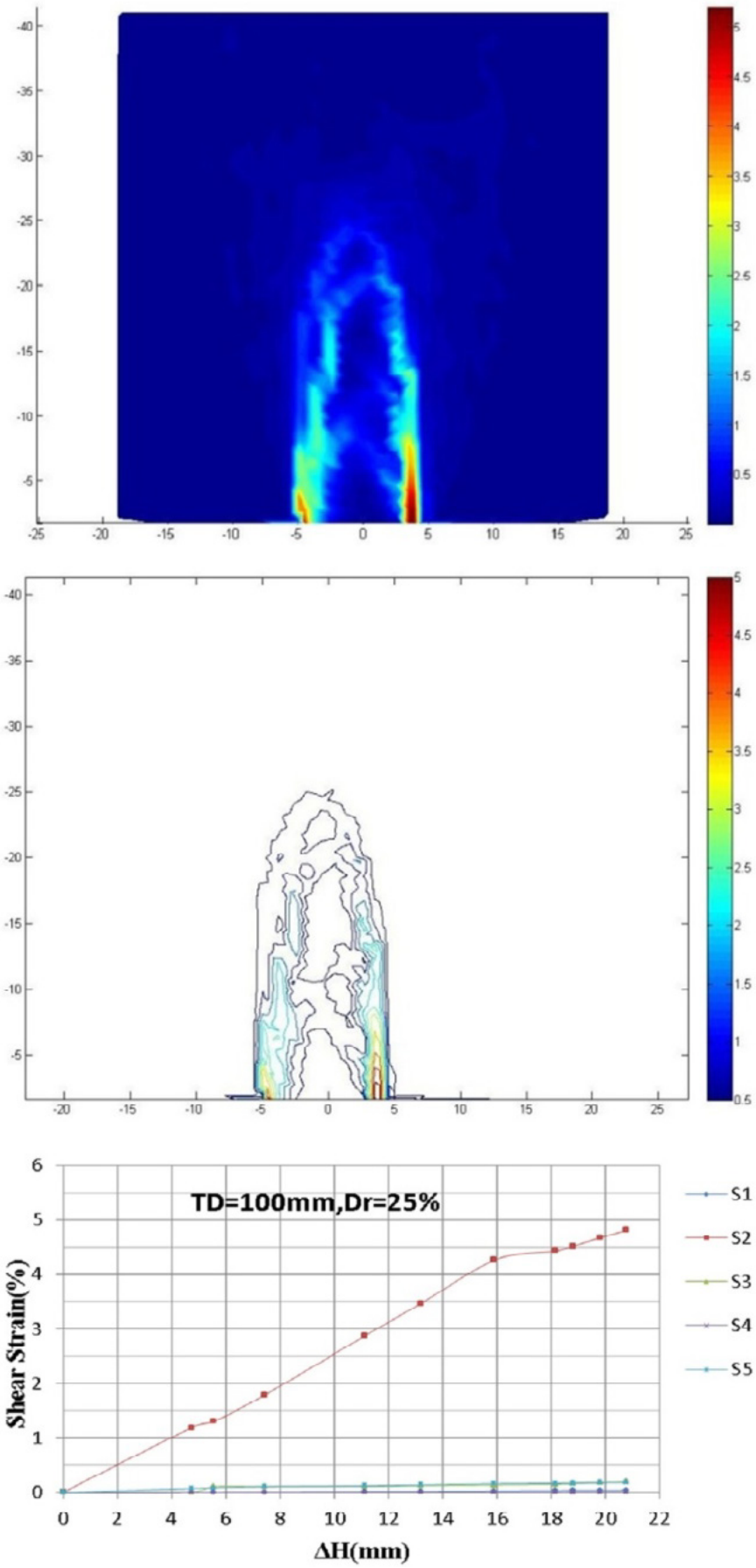

Figure 19. The results of PIV method for a valve with a width of 10 cm and a relative density of 25% .

https://doi.org/10.17993/3ctic.2023.122.15-58

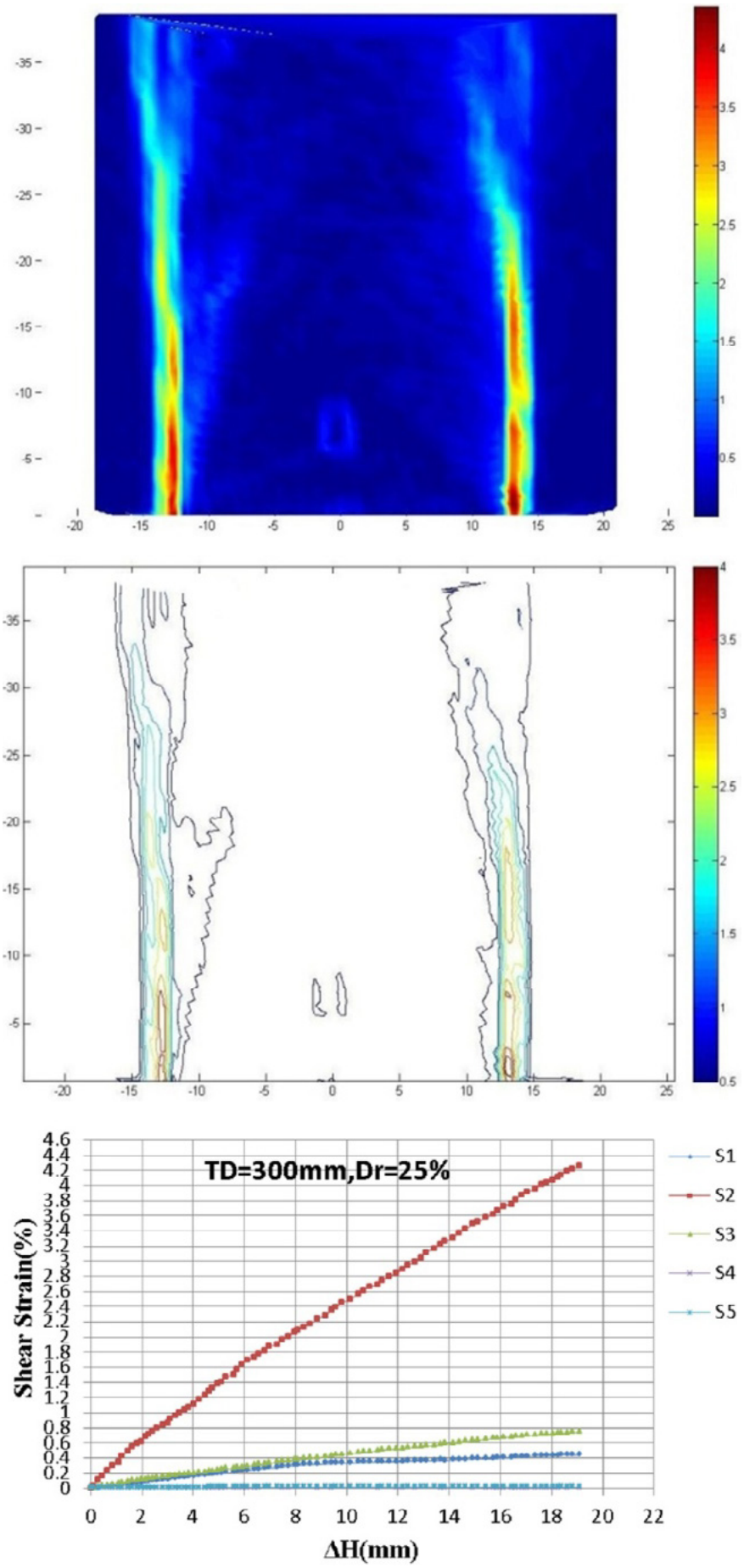

Figure 20. The results of the PIV method for a valve with a width of 30 cm and a relative density of 25%.

https://doi.org/10.17993/3ctic.2023.122.15-58

4.4. THE RESULTS OF STRAIN ANALYSIS

Based on the results of experiments and numerical modeling, after the occurrence of the arch phenomenon, four separate areas can be distinguished in terms of the behavior of the sand mass.

The first area: In this area, the soil mass behaves elastically, and the sand mass moves in general, and the particles do not have any relative movement to each other.

The second area: In the second area, a shear band is formed, and during the expansion of the arch phenomenon, it develops towards the crown of the arch, and the sand shows softening behavior.

The third area: the stresses in this area increased with the development of the arch phenomenon, and the sand mass shows hardening behavior. This area acts as a column to transfer stress to the foundation. Of course, this area is moved to the sides with the movement of the valve, and its position depends on the rate of motion of the valve.

The fourth area: This part has not been affected by the arching phenomenon, and the stresses and strains in this area remain almost constant during the arching phenomenon.

These four areas are shown in Fig. 21 .

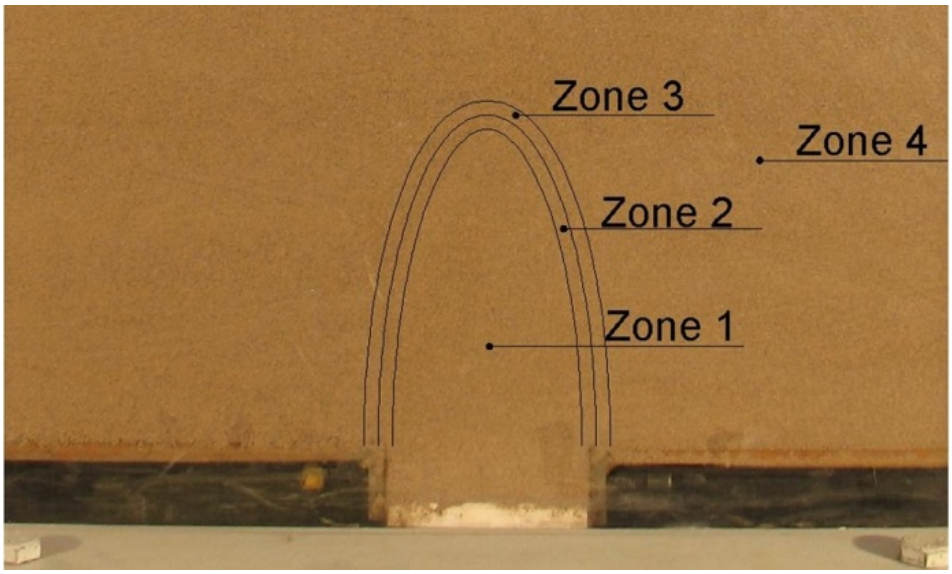

Figure 21. Four separate areas in terms of the behavior of the sand mass

5. THE NATURE OF THE FLOW PHENOMENON IN THE ARCING PHENOMENON

As mentioned, when the valve starts to move downward, a sharp and rapid drop in the amount of stress on the valve is immediately observed, which is due to the

https://doi.org/10.17993/3ctic.2023.122.15-58

transfer of stresses to the fixed sides in the range of elastic strain. Then, by minimizing the stress on the valve by moving it more and applying more strains to the soil, the amount of stress on the valve does not change, and the stress remains constant in a wide range of plastic strains, especially at the edges of the valve. This phenomenon is called flow, which isn't associated according to the definition of the expansion angle dependent on plastic strain in numerical modeling and the acceptable agreement of the results of the numerical model with the results of the experiments. Also, the phenomenon of flow and application of large strains, which is the nature of the arch phenomenon in the sand, is well modeled in the finite element method, in Fig. 22, these large deformations in the elements can be seen well.

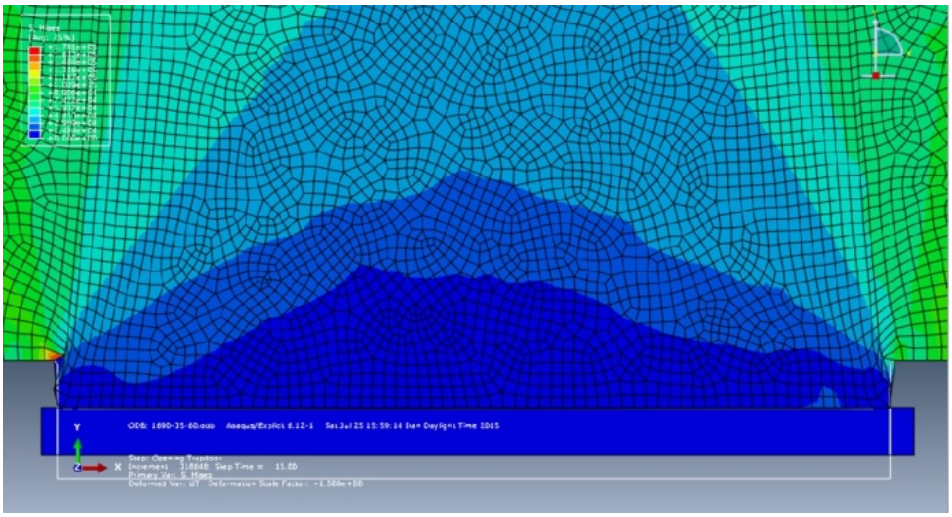

Figure 22. Large deformations applied to the elements in the finite element method

6. TENSION SPACE IN THE SELECTED BEHAVIORAL MODEL

The selected behavioral model for numerical analysis can be divided into two separate parts, elastic and plastic. In the flexible section, with the increase in the stress level, the modulus of elasticity increases until the sand reaches the yield point. When the sand comes to the yield point, the plastic stage begins, and the behavior leaves the elastic region. In the plastic area, depending on the plastic strain rate, there are two behaviors hardening and softening. According to the mentioned zoning, depending on the position considered for it, in each of the areas, the sand element can have a hardening or softening behavior or both behaviors. In the numerical model, according to the definition of the plane strain state, the stress path at different points is obtained using the following relations.

Plain Strain;

$$\varepsilon_2 = 0$$

$$p' = \frac{\sigma'_1 + \sigma'_2 + \sigma'_3}{3} \quad \text{and} \quad p = \frac{\sigma_1 + \sigma_2 + \sigma_3}{3}$$

https://doi.org/10.17993/3ctic.2023.122.15-58

$$p' = p - u$$

$$q = q' = \frac{1}{\sqrt{2}}\left[\left(\sigma_1' - \sigma_3'\right) + \left(\sigma_1' - \sigma_3'\right) + \left(\sigma_1' - \sigma_3'\right)\right]^{1/2}$$

$$\varepsilon_p = \varepsilon_1 + \varepsilon_3$$

$$\varepsilon_q = \frac{2}{3}\left(\varepsilon_1^2 + \varepsilon_3^2 - \varepsilon_1\varepsilon_3\right)^{1/2}$$

As stated in the previous sections, four separate areas can be distinguished in the arcing phenomenon. These areas are shown in Fig. 17. To investigate the approach to stress in each area, a point has been selected, and the approach to stress in these points has been discussed. For example, numerical modeling results have been chosen for a relative density of 25% and a valve width of 10 cm.

6.1. THE STRESS SPACE OF AREA 1 (ELASTIC AREA)

In Fig. 23, the diagram related to the path of stress in the space of P and q is presented at a point located in zone 1 in a valve with a width of 10 cm and a relative density of 25%. Also, in Fig. 23, specific volume changes in P and v space are shown.

According to Fig. 22, P and q decrease rapidly at the beginning of the experiment. After reaching a minimum value, the reduction rate of q decreases, and the sand enters the flow phenomenon. In the range of occurrence of the flow phenomenon, the value of q has decreased much less, while the rate of decrease of p is very high. As the valve continues to go down, the average and shear stresses start to decrease again, this process continues until the end of the test, until it finally reaches a constant value in the shear stress. This is although the specific volume has not changed much during the trial and is almost constant. In the area of a mass of sand, it is entirely and without strain changed by the displacement of the valve, and the average and shear stresses are reduced at different rates depending on the amount of displacement of the valve. It can be said that Region 1 remains in the elastic range due to the meager amount of strains generated during the arch phenomenon, and only changes in the modulus of elasticity depending on the stress level are effective in this range.

In the graphs related to Figs. 23 and 24, the direction of the arrow represents the direction of changes in stresses and specific volume during the test.

https://doi.org/10.17993/3ctic.2023.122.15-58

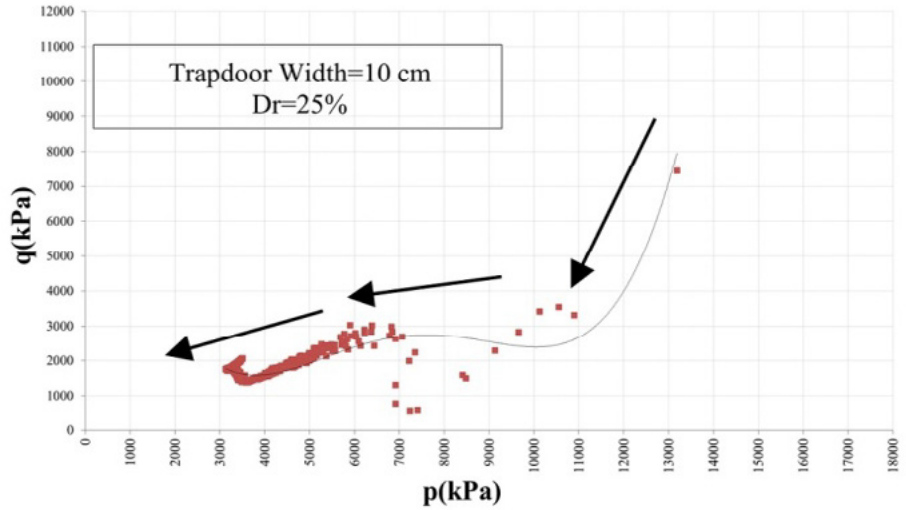

Figure 23. Diagram of stress path in p and q space for the point located in area 1

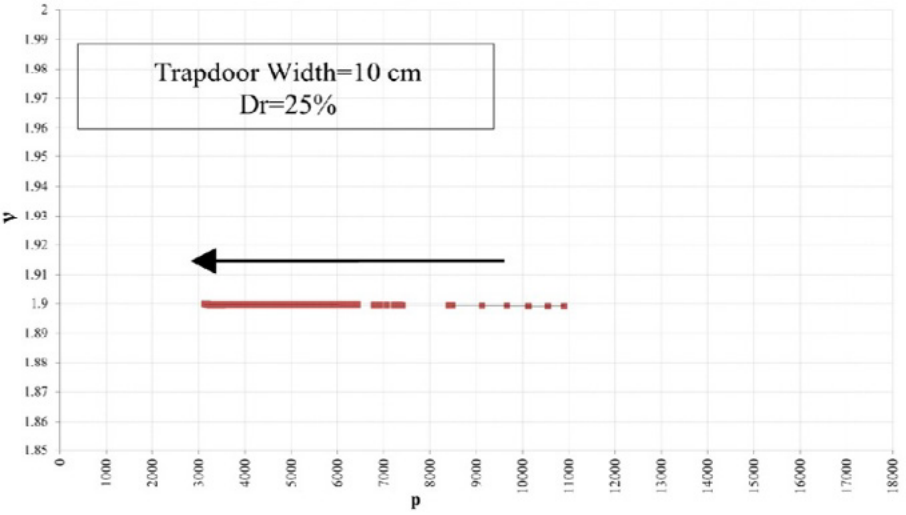

Figure 24. Diagram of stress path in p and v space for the point located in area 1

6.2. THE STRESS SPACE OF ZONE 2 (SOFTENING ZONE)

In Fig. 25, the diagram related to the path of stress in the space of P and q is presented at a point located in the expansion of the plastic points and the place of rupture (region 2) in the valve with a width of 10 cm and a relative density of 25%. Also, in Fig. 25, specific volume changes in P and v space are presented.

According to Fig. 25, P and q decrease rapidly at the beginning of the experiment. After reaching a specific value, the reduction rate of q is reduced due to the phenomenon of flow, the rate of extreme changes is related to the average stress. In the area where the flow phenomenon occurs, the value of q has decreased much less, while the rate of decrease of p is very high. As the valve goes down, the stresses continue in a straight line and on the critical line (CSL) until the end of the test. In this area, according to the diagram presented in the plastic strain range, the sand shows a softening behavior on the critical state line with an almost constant

https://doi.org/10.17993/3ctic.2023.122.15-58

slope that can be calculated from the internal friction angle of the sand in the residual state, the path continues itself. In Fig. 26, with the beginning of the test and with the reduction of the average stress, the specific volume increases upon reaching the critical line, and the rate of growth in the particular volume increases until it reaches the maximum value. In fact, in this diagram, in the area where the flow phenomenon occurs, the specific volume change rate is much lower than in other areas.

In the graphs related to Figs. 25 and 26, the direction of the arrow represents the direction of changes in stresses and specific volume during the test.

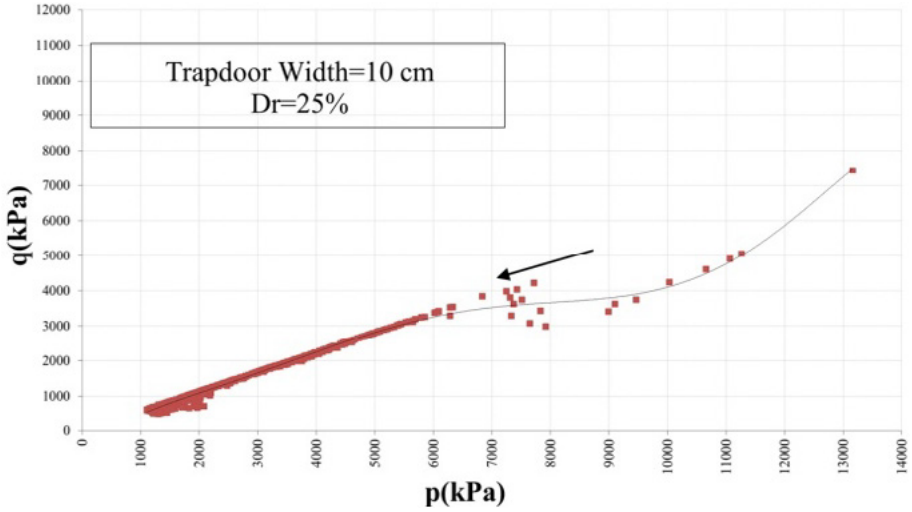

Figure 25. Diagram of stress path in p and q space for the point located in area 2

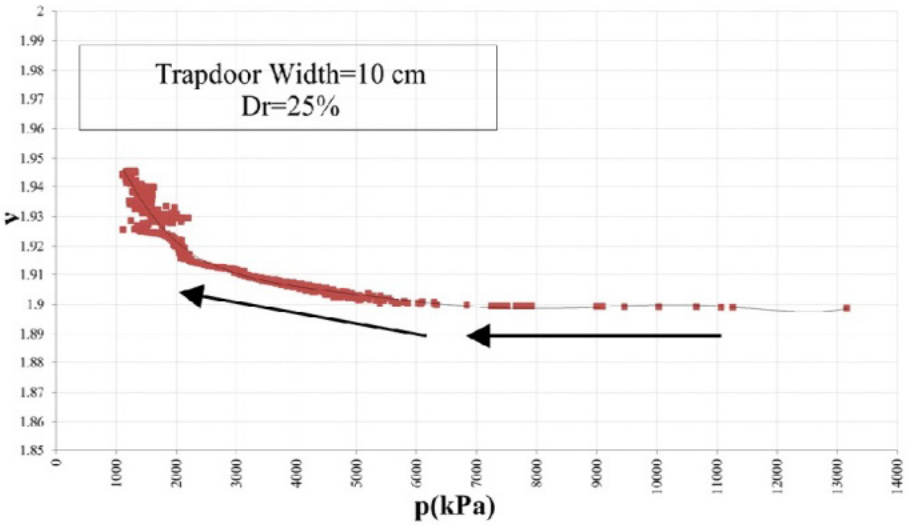

Figure 26. Diagram of stress path in p and v space for the point located in area 2

6.3. THE STRESS SPACE OF THE AREA NEAR THE VALVE (HARDENING AND SOFTENING EXPANSION AREA)

In Fig. 27, the diagram related to the path of stress in the space of P and q is presented at a point located in the area of expansion of hardening and softening

https://doi.org/10.17993/3ctic.2023.122.15-58

(region 3 - areas near the valve) for a valve with a width of 10 cm and a relative density of 25%. Also, in Figure 28, specific volume changes in P and v space are shown.

In Fig. 27, with the start of the test and moving the valve, and transferring the stresses to the fixed parts of the model, the stresses P and q increase, this stress transfer leads to the occurrence of hardening behavior in the sand, and this process continues until reaching the ultimate point, after reaching the ultimate point, the average and shear stresses decrease, and the sand shows a softening behavior. It can be seen in Fig. 28 that the specific volume is almost constant at the beginning of the test, and near the maximum point of the average stress, the specific volume increases. After the ultimate point of moderate stress, the increase rate of specific volume increases as it decreases. In the graphs related to Figs. 27 and 28, the direction of the arrow represents the direction of changes in stresses and specific volume during the test.

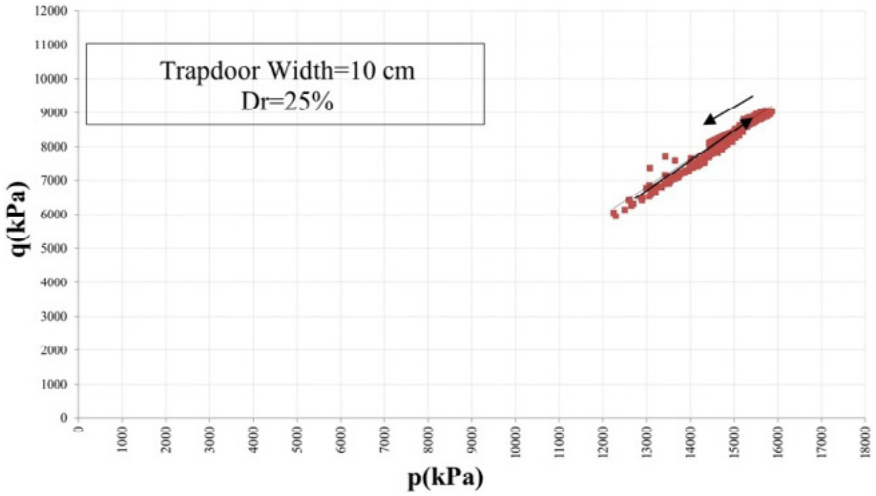

Figure 27. Diagram of stress path in p and q space for the point located in area 3 - areas near the valve

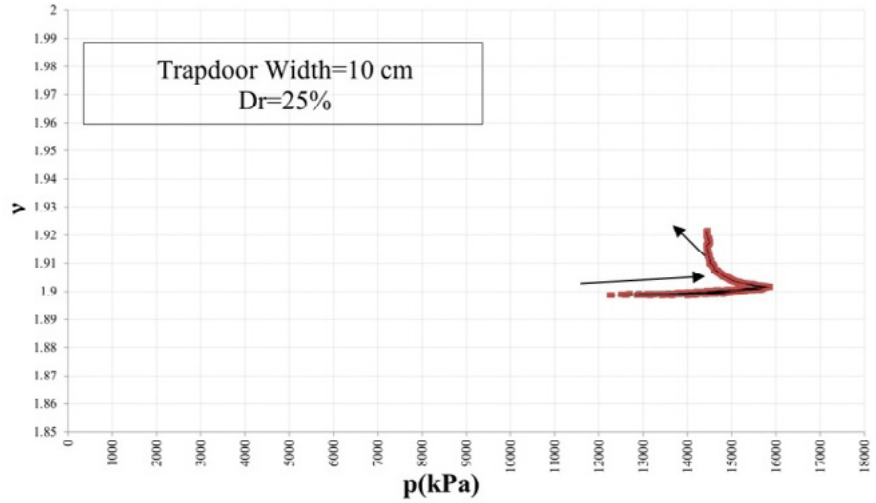

Figure 28. Diagram of the path of stress in p and v space for the point located in area 3 - areas near the valve

https://doi.org/10.17993/3ctic.2023.122.15-58

6.4. THE STRESS SPACE OF ZONE 3 (HARDENING ZONE) - FARTHER FROM THE VALVE

In Fig. 29, the graph related to changes in the stress path in the environment p and q for the point located in the hardening area (area 3 - areas far from the valve) is presented. As you can see, as the valve goes down, the amount of average stress and shear stress increases. With the increase of moderate and shear stresses, the value of specific volume decreases (Fig. 30). Of course, this reduction in particular volume is minimal. In this area, sand exhibits elastic and plastic hardening behavior. So that in the flexible region, it is related to the hardening caused by the increase in the modulus of elasticity, which is dependent on the stress level, in the plastic region, it is related to the hardening caused by the increase in the internal friction angle, which is dependent on the plastic strain. In the graphs related to Figs. 29 and 30, the direction of the arrow represents the direction of changes in stresses and specific volume during the test.

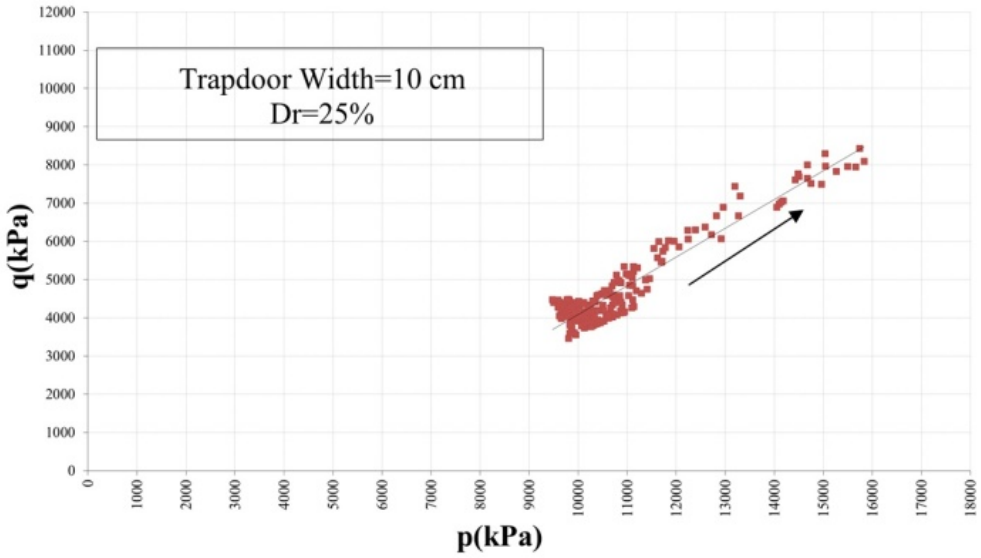

Figure 29. Diagram of stress path in p and q space for the point located in area 3 - areas far from the valve

https://doi.org/10.17993/3ctic.2023.122.15-58

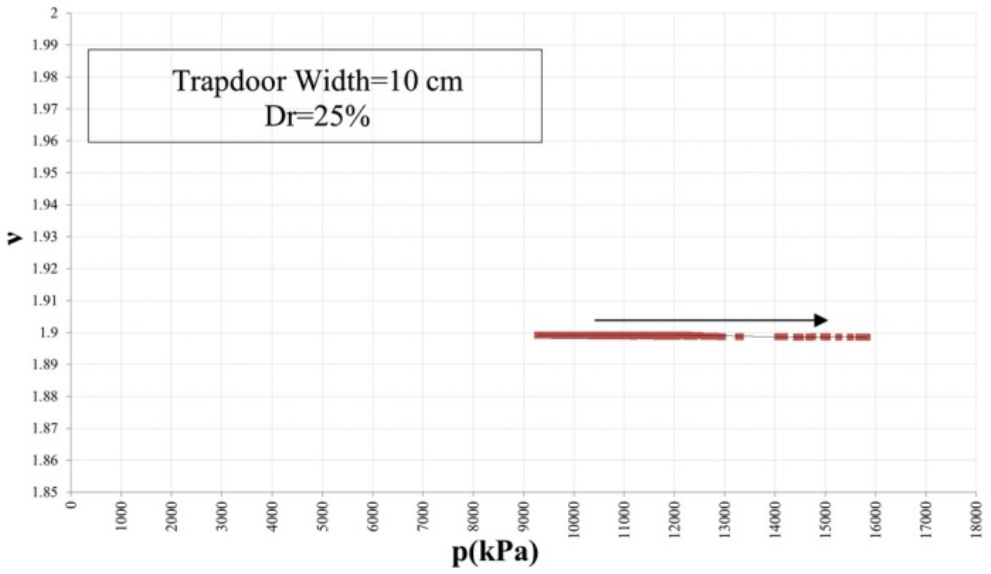

Figure 30. Diagram of stress path in p and v space for the point located in region 3 - regions far from the valve

7. CONCLUSION

Based on the studies conducted in this research, the following can be stated as the main results:

1. Four distinct phases can be distinguished in the arcing phenomenon:

   • The first phase: This phase starts immediately after the start of the valve drop, so that the tension applied to the valve is immediately and strongly reduced and reaches the minimum value. In this phase, the soil behaves elastically, and the deformations are small, while the stress changes are huge. At the beginning and before moving the valve, the shear stress values in the sand mass and around the valve are zero, and the principal stresses are vertical and horizontal. As the valve begins to move around the arch area, the shear stress starts to increase, and as a result, the principal stresses deviate from the vertical and horizontal state and rotate. In fact, in this phase, in arc development, the principal stress plane turns by creating shear stresses. So that the value of the principal stresses is reduced to the minimum and the principal stresses are increased to the maximum. In other words, the diameter of Mohr's circle increases in the arched area. This process of changes in the plane of principal stresses continues until the formation of a stable arch.

   • The second phase: This phase begins after the minimum stress point. This phase occurs in a wide range of valve displacement and the range of development of plastic strains. In the second phase, the plastic strains, and finally, the rupture starts from the side of the valve and proceeds in the direction perpendicular to the two ends of the valve

https://doi.org/10.17993/3ctic.2023.122.15-58

towards the surface. Convergence or divergence of this development of plastic strains and rupture depends on the density of the soil and the width of the valve, which determines the stable or unstable arch. In this phase, the phenomenon of flow occurs in the soil mass, so that despite high strains, there is no significant change in the applied stress on the valve.

• The third phase: This phase begins with an increase in the applied tension on the valve. At this stage, the separation and formation of a stable arc take place. If there is no stable arc, the rising trend of tension continues.

• Fourth phase: In this phase, the total weight of the stable arc is applied on the tension gauge, and the applied tension on the valve remains almost constant. In case of an unstable arc in this phase, the tension will be steady and increasing.

2. Based on the results of experiments and numerical modeling, after the occurrence of the arch phenomenon, four separate areas can be distinguished in terms of the behavior of the sand mass :

• The first area: In this area, the soil mass behaves elastically, so that the mass moves as a whole and the particles do not have any relative movement with each other, that is, the amount of strains in this area is minimal.

• The second area: In the second area, a shear band is formed, and during the expansion of the arch phenomenon, it develops towards the crown of the arch, and the sand shows softening behavior.

• The third area: the stresses in this area increased with the development of the arch phenomenon, and the sand mass shows hardening behavior. This area acts as a column to transfer stress to the foundation. Of course, this area is moved to the sides with the displacement of the valve, and its position depends on the displacement of the valve.

• The fourth area: this part has not been affected by the arch phenomenon, and the stresses and strains remain almost constant during the occurrence of the arch phenomenon.

3. Due to the wide application of the simple straight-cut test and the ease of performing this test, the resistance parameters obtained from the simple straight-cut test can be used with acceptable accuracy for the numerical modeling of the arcing phenomenon.

https://doi.org/10.17993/3ctic.2023.122.15-58

4. The best behavioral model governing the phenomenon can be defined as follows:

   • Elastic part: hardening depending on the stress level by defining the change of the modulus of elasticity against the stress change.

   • Plastic part: Hardening depending on the plastic strain up to the peak point (peak) by defining the increase of the internal friction angle up to the peak internal friction angle and softening depending on the plastic strain up to the critical limit point by defining the decrease of the internal friction angle up to the critical limit internal friction angle.

5. In the arched area, the lateral pressure coefficient of the sand is not constant and increases with the displacement of the valve. This rate of increase depends on the relative density of sand and shows an increase up to 2 times the initial value.

6. According to the definition of the expansion angle dependent on the plastic strain in numerical modeling and the acceptable agreement of the results of the numerical model with the results of the experiments, the flow in the arc phenomenon has no associated nature.

7. In examining the path of stress during the occurrence of the arch phenomenon, three separate areas can be identified in terms of changes in average and shear stress and specific volume :

   • Area 1: rapid decrease of p and q, approximate constancy of specific volume (elastic).

   • Area 2: reduction of p and q, flow phenomenon area, critical line (CSL), an increase of specific volume (softening area).

   • Area 3 and in the areas near the valve: increase and then decrease p and q, hard behavior and then softening, stability and then increase of specific volume (expansion area of hard and softening).

   • Area 3 and in areas further from the valve: increasing p and q, reducing the specific volume to a minimal amount (area of hardening) .

REFERENCES

(1) Terzaghi, K. (1943). Theoretical Soil Mechanics. John Wiley and Sons. Inc. New York, U.S.A.

(2) Janssen, H. A. (1895). "Versuche fiber Getreidedruck in Silozellen". Zeitschrift Verein Deutscher Ingenieure, Bd XXXIX, 1045-1049.

(3) Finn, W. D. L. (1963). "Boundary Value Problems of Soil Mechanics". Journal of the Soil Mechanics and Foundation Division, ASCE, Vol. 89, No. SM5, 39-72.

https://doi.org/10.17993/3ctic.2023.122.15-58

(4) Amimoto, K., Okamoto, T., & Yamada, S. (1959). "Measurement of Earth Pressure Acting on Earth Retaining Walls for-Subway-Construction". Tsuchito-Kiso, JSSMFE, Vol.7, No.4, 21.

(5) Atkinson, J. H., & Potts, D. M. (1977). Stability of a shallow circular tunnel in cohesionless soil. Geotechnique, 27(2), 203–215.

(6) Jiang, M. J., & Yin, Z. Y. (2012). Analysis of stress redistribution in soil and earth pressure on tunnel lining using the discrete element method. Tunnelling and Underground Space Technology, 32(6), 251–259.

(7) Guo, P., & Zhou, S. (2013). Arch in granular materials as a free surface problem. International Journal of Numerical Analysis and Methods in Geomechanics, 37(9), 1048–1065.

(8) Han, L., Ye, G. L., Chen, J. J., Xia, X. H., & Wang, J. H. (2017). Pressures on the lining of a large shield tunnel with a small overburden: a case study. Tunnelling and Underground Space Technology, 64, 1–9.

(9) Franza, A., Marshall, A. M., & Zhou, B. (2018). Greenfield tunnelling in sands: the effects of soil density and relative depth. Geotechnique, 1–11.

(10) Chen, K. H., & Peng, F. L. (2018). An improved method to calculate the vertical earth pressure for deep shield tunnel in Shanghai soil layers. Tunnelling and Underground Space Technology, 75, 43–66.

(11) Jin, D. L., Zhang, Z. Y., & Yuan, D. Y. (2021). Effect of dynamic cutterhead on face stability in EPB shield tunneling. Tunnelling and Underground Space Technology, 110(1), 103827.

(12) Zheng, H. B., Li, P. F., & Ma, G. W. (2021). Stability analysis of the middle soil pillar for asymmetric parallel tunnels by using model testing and numerical simulations. Tunnelling and Underground Space Technology, 108, 103686.

(13) Stein, D., Mollers, K., & Bielecki, R. (1989). Microtunnelling. Berlin, Germany: Ernest & Sohn, pp. 237–243.

(14) Handy, R. L. (1985). The arch in soil arching. Journal of Geotechnical Engineering, 111(3), 302–318.

(15) Chen, R. P., Tang, L. J., Yin, X. S., Chen, Y. M., & Bian, X. C. (2015). An improved 3D wedge-prism model for the face stability analysis of the shield tunnel in cohesionless soils. Acta Geotechnica, 10(5), 683–692.

(16) Zhang, H. F., Zhang, P., Zhou, W., Dong, S., & Ma, B. S. (2016). A new model to predict soil pressure acting on deep burial jacked pipes. Tunnelling and Underground Space Technology, 60, 183–196.

(17) Jacobsz, S. W. (2016). Trapdoor experiments studying cavity propagation. In: Proceedings of the first Southern African Geotechnical Conference, pp. 159–165.

(18) Song, J. H., Chen, K. F., Li, P., Zhang, Y. H., & Sun, C. M. (2018). Soil arching in unsaturated soil with different water table. Granular Matter, 20(4), 78.

(19) Chen, R. P., Yin, X. S., Tang, L. J., & Chen, Y. M. (2018). Centrifugal model tests on face failure of earth pressure balance shield induced by steady-state seepage in saturated sandy silt ground. Tunnelling and Underground Space Technology, 81, 315–325.

https://doi.org/10.17993/3ctic.2023.122.15-58

(20) Lin, X. T., Chen, R. P., Wu, H. N., & Cheng, H. Z. (2019). Three-dimensional stress-transfer mechanism and soil arching evolution induced by shield tunneling in sandy ground. Tunnelling and Underground Space Technology, 93.

(21) Chen, R. P., Lin, X. T., & Wu, H. N. (2019). An analytical model to predict the limit support pressure on a deep shield tunnel face. Computers and Geotechnics, 115, 103174.

(22) Costa, Y. D., Zornberg, J. G., Bueno, B. S., & Costa, C. L. (2009). Failure mechanisms in sand over a deep active trapdoor. Journal of Geotechnical and Geoenvironmental Engineering, 135(11), 1741–1753.

(23) Wu, J., Liao, S. M., & Liu, M. B. (2019). An analytical solution for the arching effect induced by ground loss of tunneling in sand. Tunnelling and Underground Space Technology, 83, 175–186.

(24) Adrian, R. J. (1991). Particle imaging techniques for experimental fluid mechanics. Annual Review of Fluid Mechanics, 23, 261–304.

(25) White, D. J., Take, W. A., & Bolton, M. D. (2003). Soil deformation measurement using particle image velocimetry (PIV) and photogrammetry. Geotechnique, 53(7), 619–631.

(26) ABAQUS 2012 User's Documentation, Hibbit, Karlsson and Sorensen, Inc.

(27) Shibuya, S., Mitachi, T., and Tamate, S. (1997). Interpretation of direct shear box testing of sands as quasi-simple shear. Geotechnique, 47(4), 769–790.

(28) Davis R. O., & Selvadurai, A. P. S. (2002). Plasticity and Geomechanics. Cambridge University Press

https://doi.org/10.17993/3ctic.2023.122.15-58